56 Sparta Avenue • Newton, New Jersey 07860
(973) 300-3000 Sales • (973) 300-3600 Fax
www.thorlabs.com

THORLABS

<div style="border: 2px solid red">

AOK2-UM01 - May 13, 2015

Item # AOK2-UM01 was discontinued on May 13, 2015. For informational purposes, this is a copy of the website content at that time and is valid only for the stated product.

</div>

ADAPTIVE OPTICS KITS

► **Kit Includes Deformable Mirror, Shack-Hartmann Wavefront Sensor, and All Necessary Optics / Hardware**
► **>190 Hz Closed-Loop Operation with Fast CMOS Wavefront Sensor**
► **Closed-Loop Operation via Stand-Alone Control Software**

Shack-Hartmann Wavefront Sensor
CCD-Based

Deformable Mirror
6x6 or 12x12 Array

Shack-Hartmann Wavefront Sensor
CMOS-Based

Hide Overview

OVERVIEW

Features

- Complete Kit and Software for Out-of-the-Box Wavefront Measurement and Control
- Kit Includes (See the *Components* Tab for Details):
  - Continuous Suface Deformable Mirror
  - Shack-Hartmann Wavefront Sensor
  - Laser Diode Module (635 nm)
  - All Imaging Optics and Associated Mounting Hardware
  - Fully Functional Stand-Alone Control Software for Windows
  - SDK for Custom Applications Authored by the End User
- Five Kits Available with the Following Options:
  - Aluminum- or Gold-Coated Deformable Mirror
  - 32- (Gold Only) or 140-Actuator Deformable Mirror
  - 15 Hz CCD or 880 Hz (Max) CMOS Shack-Hartmann Wavefront Sensor
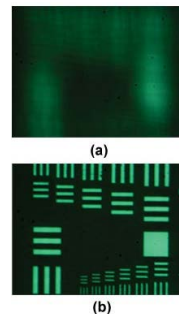
(a)

(b)

Resolution target imaged using (a) a flat mirror (b) an optimized deformable mirror. The smallest lines are separated by 2 μm.

Each Thorlabs' adaptive optics kit is a complete adaptive optics imaging solution, including a deformable mirror, wavefront sensor, control software, and optomechanics for assembly. These precision wavefront control devices are useful for beam shaping, microscopy, laser communications, and retinal imaging as well as educational demonstrations. To learn more how the wavefront sensor, deformable mirror, and software operate as a closed-loop system to correct wavefront distortion, please see the various tabs on this page or the Adaptive Optics 101 white paper.

Thorlabs now offers five variations of our AO Kits. First, choose from a gold- or aluminum-coated deformable mirror with 140 or 32 actuators (32 actuator version available with a gold coating only). Then, choose between a 15 Hz CCD-based or a high-speed 880 Hz (max) CMOS-based Shack-Hartmann wavefront sensor. Details on all five AO Kit options are outlined in the various tabs on this page. A reflectance plot for the gold and aluminum coatings is available on the *DM* tab.

Related White Papers		
Adaptive Optics 101	Linear Array Deformable Mirror	MEMS Optical Modulator

Hide Specs

SPECS

Item #	AOK1-UM01	AOK1-UP01	AOK5-UM01	AOK5-UP01
Boston Micromachines Deformable Mirror				
Deformable Mirror Type	Multi-DM			
Deformable Mirror Item #	DM140A-35-UM01	DM140A-35-UP01	DM140A-35-UM01	DM140A-35-UP01
Actuator Array	12 x 12			
Actuator Count	140			

Actuator Stroke (Max)	3.5 µm			
Actuator Pitch	400 µm			
Clear Aperture	4.4 mm x 4.4 mm			
Mirror Coating (Click for Plot)	Gold	Aluminum	Gold	Aluminum
Mirror Wavelength Range	600 - 1100 nm	400 - 1100 nm	600 - 1100 nm	400 - 1100 nm
Surface Quality	<30 nm RMS			
Average Step Size	<1 nm			
Hysteresis	None			
Fill Factor	>99%			
Mechanical Response Time (10% - 90%)	<100 µs (~3.5 kHz)			
Interactuator Coupling, CDM	20% - 40%			
Head Dimensions	Ø2" x 0.89" (Ø50.8 mm x 22.5 mm)			
Frame Rate (Max)	8 kHz (34 kHz Bursts)			
Resolution	14 Bit			
Driver Dimensions	9.0" x 7.0" x 2.5" (229 mm x 178 mm x 64 mm)		4.0" x 5.25" x 1.25" (102 mm x 133 mm x 32 mm)	
Computer Interface	USB 2.0			

Thorlabs' Shack-Hartmann Wavefront Sensors		
Wavefront Sensor Type	CCD-Based Sensor	CMOS-Based Sensor
Wavefront Sensor Item #	WFS150-5C	WFS20-5C
Frame Rate (Max)	15 Hz[a]	880 Hz
Aperture Size (Max)	5.95 mm x 4.76 mm (Set at 3.7 mm x 3.7 mm)	7.20 mm x 5.40 mm
Camera Resolution (Max)	1280 x 1024 Pixels (Set at 768 x 768)	1440 x 1080 Pixels, Selectable
Pixel Size	4.65 x 4.65 µm	5.0 x 5.0 µm
Shutter	Global	
Exposure Range	77 µs - 66 ms	4 µs - 83.3 ms
Wavelength Range	300 - 1100 nm	
Lenslet Pitch	150 µm	
Lenslet Diameter	146 µm	
Number of Lenslets (Max)	39 x 31 (Set at 21 x 21)	47 x 35
Effective Focal Length	3.7 mm	
Substrate	Fused Silica (Quartz)	
Coating	Chrome Mask	
Wavefront Accuracy @ 633 nm	λ/15 rms	λ/30 rms
Wavelength Sensitivity @ 633 nm	λ/50 rms	λ/100 rms
Wavefront Dynamic Range @ 633 nm	>100λ	
Local Radius of Curvature	>7.4 mm	
Image Digitization	8 Bit	
Warm-Up Time for Rated Accuracy	15 minutes	
Optical Input Connector	C-Mount (1.000"-32.0)	
Physical Size (H x W x D)	34.0 mm x 32.0 mm x 48.5 mm (1.34" x 1.26" x 1.91")	56.0 mm x 46.0 mm x 28.3 mm (2.20" x 1.81" x 1.11")
Power Supply	<1.5 W via USB	External; 12 V DC, 1.5 A
Operating and Storage Temperature	5 to 35 °C (Operating) / -40 to 70 °C (Storage)	

Item #	AOK2-UM01
Boston Micromachines Deformable Mirror	
Deformable Mirror Type	Mini-DM
Deformable Mirror Item #	DM32-35-UM01
Actuator Array	6 x 6
Actuator Count	32
Actuator Stroke (Max)	3.5 µm
Actuator Pitch	400 µm
Clear Aperture	2.0 mm x 2.0 mm
Mirror Coating (Click for Plot)	Gold (-UM01)
Mirror Wavelength Range	600 - 1100 nm
Surface Quality	<20 nm RMS
Average Step Size	<1 nm
Hysteresis	None
Fill Factor	>99%
Mechanical Response Time (10% - 90%)	<100 µs (~3.5 kHz)
Interactuator Coupling, CDM	20% - 40%
Head Dimensions	4.5" x 2.95" x 2.8" (114.3 mm x 74.9 mm x 71.1 mm)
Frame Rate (Max)	8 kHz (34 kHz Bursts)
Resolution	14 Bit
	4.0" x 5.25" x 1.25"

Driver Dimensions	(102 mm x 133 mm x 32 mm)
Computer Interface	USB 2.0
Thorlabs' Shack-Hartmann Wavefront Sensors	
Wavefront Sensor Type	CCD-Based Sensor
Wavefront Sensor Item #	WFS150-5C
Frame Rate (Max)	15 Hz[a]
Aperture Size (Max)	5.95 mm x 4.76 mm (Set at 3.7 mm x 3.7 mm)
Camera Resolution (Max)	1280 x 1024 Pixels (Set at 768 x 768)
Pixel Size	4.65 x 4.65 µm
Shutter	Global
Exposure Range	77 µs - 66 ms
Wavelength Range	300 - 1100 nm
Lenslet Pitch	150 µm
Lenslet Diameter	146 µm
Number of Lenslets (Max)	39 x 31 (Set at 21 x 21)
Effective Focal Length	3.7 mm
Substrate	Fused Silica (Quartz)
Coating	Chrome Mask
Wavefront Accuracy @ 633 nm	λ/15 rms
Wavelength Sensitivity @ 633 nm	λ/50 rms
Wavefront Dynamic Range @ 633 nm	>100λ
Local Radius of Curvature	>7.4 mm
Image Digitization	8 Bit
Warm-Up Time for Rated Accuracy	15 minutes
Optical Input Connector	C-Mount (1.000"-32.0)
Physical Size (H x W x D)	34.0 mm x 32.0 mm x 48.5 mm (1.34" x 1.26" x 1.91")
Power Supply	<1.5 W via USB
Operating and Storage Temperature	5 to 35 °C (Operating) / -40 to 70 °C (Storage)

- For the configurations used in the AO Kit, the frame rates will be nominally 8 Hz for the CCD sensor. This PC hardware-dependent speed is achieved without graphical display, assumes a 5th order Zernike fit at the specified camera resolution, and minimum exposure time.

All technical data is specified at 23 ± 5 °C and 45 ± 15% relative humidity.

[Hide DM](#)

D M

6 x 6 or 12 x 12 MEMS Deformable Mirror

- 6 x 6 (Mini-DM) or 12 x 12 (Multi-DM) Actuator Models Available
- 3.5 µm Maximum Actuator Displacement
- High-Speed Operation up to 3.5 kHz
- 400 µm Center-to-Center Actuator Spacing
- Low Inter-Actuator Coupling Resulting in High Spatial Resolution
- Zero Hysteresis Actuator Displacement
- 14-Bit Drive Electronics Yield Sub-Nanometer Repeatability
- Compact Driver Electronics with Built-In High-Voltage Power Supply Suitable for Benchtop or OEM Integration

Included Deformable Mirror			
Item #	Actuator Array	Mirror	Coating
AOK1-UM01	12 x 12	DM140A-35-UM01	Gold
AOK1-UP01		DM140A-35-UP01	Aluminum
AOK2-UM01	6 x 6	DM32-35-UM01	Gold
AOK5-UM01	12 x 12	DM140A-35-UM01	Gold
AOK5-UP01		DM140A-35-UP01	Aluminum

Click to Enlarge
12 x 12 Actuator
Multi DM
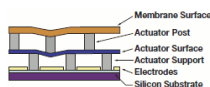
Click to Enlarge
6 x 6 Actuator
Mini DM

Through our partnership with Boston Micromachines Corporation (BMC), Thorlabs is pleased to offer BMC's Mini- and Multi- Deformable Micro-electro-mechanical (MEMS) based mirrors as part of our adaptive optics kits. These deformable mirrors (DMs) are ideal for advanced optical wavefront control; they can correct monochromatic aberrations (spherical, coma, astigmatism, field curvature, or distortion) in a highly distorted incident wavefront. MEMS deformable mirrors are currently the most widely used technology in wavefront shaping applications given their versatility, maturity of technology, and the high resolution wavefront correction capabilities they provide.
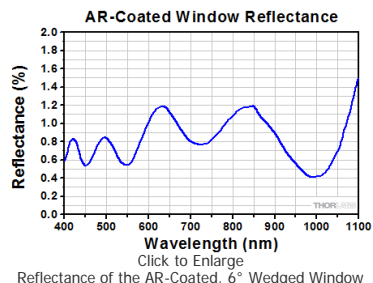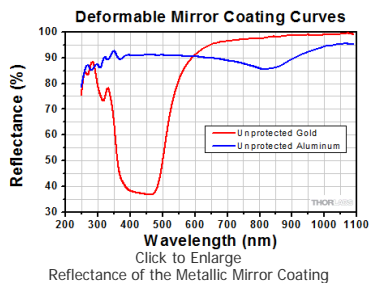
MEMS Deformable Mirror Structure
Click to Enlarge

Our Deformable Mirrors, fabricated using polysilicon surface micromachining fabrication methods, offer sophisticated aberration compensation in easy-to-use packages. The mirror consists of a mirror membrane that is deformed by either 32 electrostatic actuators (i.e., a 6 x 6 actuator array with four inactive corner actuators for the Mini-DM) or 140 electrostatic actuators (i.e., a 12 x 12 actuator array with four inactive corner actuators for the Multi-DM). These actuators provide 3.5 µm of stroke (over 11 waves at 632.8 nm) with zero hysteresis.

Mirrors are available with a Gold (-M01) or Aluminum (-P01) reflective coating (see table above for options). Each mirror is protected by a 6° wedged window that has a broadband AR coating for the 400 - 1100 nm range. See the coating curve graphs below for details. Custom coatings are available for the protective window; please contact Tech Support for more information.

BMC's Mini- and Multi-DMs are also available separately. Click here for more information.

Deformable Mirror Coating Curves

Click to Enlarge
Reflectance of the Metallic Mirror Coating

AR-Coated Window Reflectance

Click to Enlarge
Reflectance of the AR-Coated, 6° Wedged Window

Hide WFS

W F S

Shack-Hartmann Wavefront Sensor

- CCD-Based or High-Speed CMOS-Based Wavefront Sensors Available
- Wavelength Range: 300 - 1100 nm
- Real-Time Wavefront and Intensity Distribution Measurements
- Nearly Diffraction-Limited Spot Size
- For CW and Pulsed Light Sources
- Flexible Data Export Options (Text or Excel)
- Live Data Readout via TCP/IP

Item # Prefix	Wavefront Sensor Included
AOK1	15 Hz CCD, λ/50 Sensitivity Model
AOK2	WFS150-5C
AOK5	880 Hz CMOS, λ/100 Sensitivity Model WFS20-5C
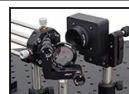
Click to Enlarge
λ/100 Sensitivity High-Speed CMOS Wavefront Sensor

Click to Enlarge
λ/50 Sensitivity CCD Wavefront Sensor

Thorlabs AO Kits include either the WFS150-5C CCD-based or the WFS20-5C high-speed CMOS-based Shack-Hartmann wavefront sensor. These Shack-Hartmann wavefront sensors can detect distortions in the wavefront which can then be corrected by the deformable mirror.

15 Hz CCD Sensor
Our WFS150-5C 1.3 Megapixel wavefront sensor has a wavefront sensitivity of up to λ/50 RMS thanks to the high spatial resolution of the CCD sensor (4.65 μm pixel pitch). This sensor operates at a frame rate of 15 Hz, and is included with the AOK1 and AOK2 AO Kits.

880 Hz High-Speed CMOS Sensor
Our WFS20-5C high-speed wavefront sensor operates at frame rates as high as 880 Hz and has a wavefront sensitivity of up to λ/100 RMS (5.0 μm pixel pitch). This sensor is included with the AOK5 AO Kits.

Thorlabs' CCD-Based and CMOS-Based wavefront sensors are also available separately.

Hide Software

## S O F T W A R E

Application Software

For out-of-the-box operation, the AO Kit comes with a fully functional, stand-alone, Windows XP and 7-compatible program for immediate operation of the instrument. This software is capable of minimizing wavefront aberrations by analyzing the signals from the Shack-Hartmann wavefront sensor and generating a voltage set that is applied to the deformable mirror. Users can also monitor the deformable mirror actuator control voltages, wavefront corrections, and intensity distribution in real time. Since the application software provides full control of the AO Kit, it is an excellent tool for research and development or developing educational packages based on adaptive optics. A software development kit is also included for custom applications (see below).

Click to Enlarge

Deformable Mirror Control

- Real-Time Representation of the Deformable Mirror Actuator Displacements (Based on Voltages Applied to the Mirror)
- Spreadsheet-Like Numerical Interface Provides User-Input of Actuator Deflections
- Save/Recall Mirror Surface Maps
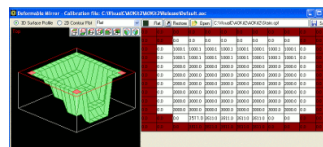
The deformable mirror control shows a graphical plot of the DM surface shape as well a spreadsheet-like numerical interface that allows the user to input actuator deflections (in nanometers). The actuator deflection values may be changed individually or in selected groups. The actual shape of the DM will differ slightly due to a small influence of adjacent actuators.

Click to Enlarge
Deformable Mirror Control

Specific mirror shapes can be loaded and saved from this window, allowing the creation of a library of unique and specialized mirror shapes that can be later recalled at the click of a button.

Shack-Hartmann Control

- Four Tab Displays
  - Wavefront Sensor Spot Field Measured Directly from the Sensor
  - Wavefront Plot (See Example at Right)
  - Contour Wavefront Plot
  - Measured Zernike Coefficients
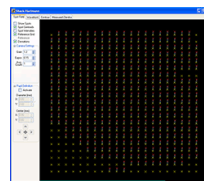- Wavefront Plot is Scalable / Rotatable
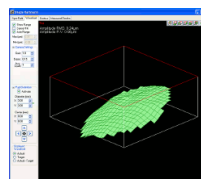
Click to Enlarge
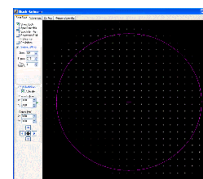
Click to Enlarge

- Easily Access Wavefront Sensor and Display Control Settings in Each Tab Display
- Display Measured, Reference, or Difference Wavefront Plots
- Min/Max Threshold Eliminates 'Flickering' Active/InactiveWFS Spots
- User-Controllable Spot Centroid and Reference Spot Indicators (See Example to the Right)

Shack-Hartmann Wavefront   Shack-Hartmann Spot Field

In the spot field window (far right image), the camera's exposure time and gain can be controlled. A pupil control allows the user to analyze the wavefront data within a user-defined circular pupil. The camera image of the spots (white spots), spot centroid locations (red X's), reference locations (yellow X's), deviations (white lines between red and yellow X's), and intensity levels can be displayed in the spot field window, as shown in the images to the far right and the bottom right.

Click to Enlarge
Shack-Hartmann Spot Centroid
Locations, Reference Locations, and
Deviations

In addition to the camera controls mentioned above, when viewing the wavefront, the user has the option to display the measured wavefront, target (reference) wavefront, or the difference between these two wavefronts. The wavefront plot can be viewed at pre-defined angles or can be continuously adjusted by the user.

Zernike Wavefront Function Generator

- User-Controllable Reference Wavefront
- User-Defined Zernike Sampling Pupil Size and Position
- User-Defined Reference Using First 36 Zernike Terms
- User-Captured Reference Wavefront
- 3D Surface Plot or 2D Contour Plot Display
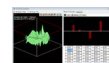
Click to Enlarge
Zernike Function
Generator

The Wavefront Generator control enables the user to create a reference wavefront by combining the first 36 Zernike polynomials in the spreadsheet-like grid. A graphical display of the created wavefront, along with the minimum, maximum, and peak-to-peak wavefront deviations are provided.

The wavefront generator control window also allows the user to capture the current measured wavefront and set it as the reference wavefront. Reference wavefronts can be saved and later recalled by the user.

Software Development Kit

The Adaptive Optics Kit includes a Software Development Kit (SDK) in the form of a flexible, cross-platform-compatible Dynamic Link Library (DLL) as well as full-featured Windows application software with an easy-to-use Graphical User Interface (GUI) for full system control right out of the box. The SDK is designed to be a conduit for easy integration of AO instrumentation, control, and arithmetic functions into a user system, making it ideal for research, development, and education applications. The application software provides immediate interaction with the AO Kit Deformable Mirror and Shack-Hartmann Wavefront Sensor and provides pop-up tooltips containing detailed information pertaining to specific function calls dispatched by the associated GUI control.

SDK Memory Management

A unique aspect of the SDK is its versatile memory structure. We provide an SDK that is compatible with a broad range of programming environments, including C-based languages, Visual Basic, LabVIEW, and any other language capable of interfacing with standard DLLs. These languages allocate data memory using different methods. In order to maximize performance and cross-platform compatibiity, the SDK employs a flexible memory structure that allows it to transparently use either its own or user software-allocated data space.

Hide Construction

CONSTRUCTION

In addition to the WFS150-5C CCD or WFS20-5C high-speed CMOS Shack-Hartmann Wavefront Sensor, your choice of an Aluminum- or Gold-Coated Mini- or Multi-DM deformable mirror, and control software (Windows XP and 7 Compatible), these adaptive optics kits also include a source, all collimation/imaging optics, and all mounting hardware necessary to build the layout depicted in Figure 1 to the right. Please note that a breadboard is not included.
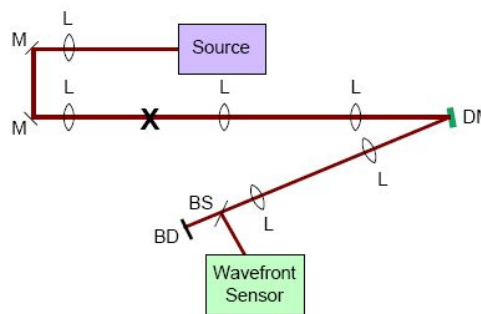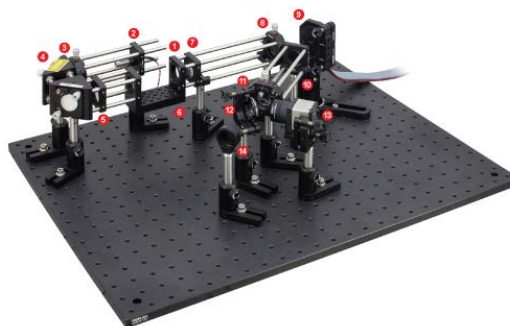
Figures 2 and 3 below are photographs showing two different views of an assembled AOK1-UM01 AO Kit. The other adaptive optics kits follow a similar layout, but contain slightly different components, as outlined in the table on the *Components* tab. The cage components are divided into three pre-aligned pieces that need to be arranged on a user-supplied breadboard: two sections of preassembled cage components are used together to image a beam waist onto the DM surface and a third preassembled cage system is used to image a beam waist onto the Shack-Hartmann wavefront sensor.

Figure 1. Schematic showing the major components included with the AOK1-UM01, AOK1-UP01, AOK2-UM01, AOK5-UM01, and AOK5-UP01 Adaptive Optics Kits. L, M, DM, BS, and BD refer to lens, mirror, deformable mirror, beamsplitter, and beam dump, respectively. The "X" marks the position of the CB1 U-bench, which is also the location of an image plane in the setup; thus, if desired, a user-supplied sample can be inserted at this location.

If you are not familiar with Thorlabs' 30 mm cage assemblies, they consist of cage-compatible components that are interconnected with Ø6 mm cage rods. This design ensures that the optical components housed inside the cage system have a common optical axis. For the setup pictured in figures 2 and 3, cage rods with lengths of 1", 1.5", 3", and 6" were used.

The first two preassembled cage sections of the AOK1-UM01 consist of the laser diode source, four 75 mm focal length lenses, two cage-compatible turning mirrors, and a U-shaped bench. The CPS180 Laser Diode Module (labeled as #1 in Fig. 2), which outputs ~1 mW of light at 635 nm, is housed inside a CP02 Cage Plate (#2

in Fig. 2) using an AD11F Ø11 mm-to-SM1 Adapter. Light exiting the module is centered within the cage system and on the surface of the DM using the adjustment knobs on the two KCB1 Right-Angle Cage-Compatible Kinematic Mounts (the first of which is labeled as #4 in Fig. 2), which house PF10-03-M01 Gold-Coated Mirrors; these mirrors offer an average reflectance of >96% from 800 nm to 20 µm. A CPA1 alignment plate, which locates a small through-hole at the exact center of a cage assembly, is used to assist with this alignment.

Two LA1608-B 75 mm focal length lenses (the first of which is housed in the CXY1 Translating Lens Mount labeled as #3 in Fig. 2 and the second of which is housed in the CP02 Cage Plate labeled as #5 in Fig. 2) are used to image a beam waist at the center of the CB1 30 mm Cage System U-Bench (represented by an X in Fig. 1 and labeled as #6 in Fig. 2 to the right). A sample can be placed in this image plane. The first lens is placed ~94 mm from the source (since the collimation optic built into the laser diode module source has a focal length of ~19 mm), and the second lens is placed in the optical path so that it is ~150 mm after the first lens. Then, during the alignment process done at Thorlabs, fine adjustments are made to the lens locations by using an SI050 Shearing Interferometer to ensure the laser beam is collimated.

Next, two more LA1608-B lenses (one is housed in the CXY1 mount labeled as #8 in Fig. 2 and the other in the CP02 mount labeled as #7 in the figure) are used to image a beam waist onto the DM (#9); by having a beam waist at the DM surface, the range of actuation needed to correct for any aberrations is minimized. All of these components are connected using ER Cage Rods to build a cage system, which ensures that a common optical axis is maintained. Since both KCB1 turning mirror mounts are internally threaded, four ERSCA Adapters must be used to connect them with cage rods. These adapters are visible in the foreground of Fig. 3.
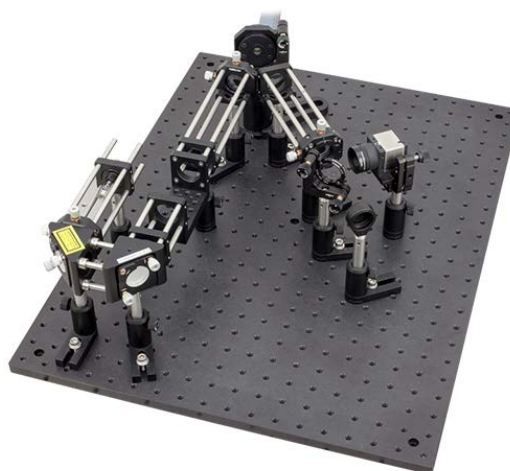
The Ø2" housing of the DM included in the AOK1-UM01 is mounted in a KS2D Kinematic Mount, which in turn is mounted on an RS2 Pillar Post and secured to the breadboard using an RSH2 Post Holder and PF175 Clamping Fork. The DM is placed on the breadboard such that it is located 75 mm after the fourth lens and so that the reflected beam makes as shallow of an angle as possible. In this case, the angle of reflection is ~35°.

The third preassembled cage section consists of two more 75 mm focal length lenses, which are once again housed using a CP02 Cage Plate (#10 in Fig. 2) and a CXY1 Translating Lens Mount (#11 in Fig. 2). Two CP02B Cage Plate Adapters, which are mounted onto TR3 Posts and secured to the breadboard using UPH2 Universal Post Holders, are placed approximately 1/3 and 2/3 of the way between the lenses to support the weight of the cage components. The lenses are used to place the DM in a plane that is conjugate with the Shack-Hartmann lenslet array, thereby enabling the AO kit software to optimize the position of the DM actuators. This section of cage components is placed on the breadboard so that the first lens is located 75 mm after the DM.

After exiting the third cage subassembly, a 92:8 pellicle beamsplitter (#12 in Fig. 2) is used to direct a small portion of the light to the last major component of the AO kit, the WFS150-5C Shack-Hartmann Wavefront Sensor (#13). The sensor is placed on a 1.6" x 1.0" Kinematic Platform Mount. The kinematic mount is threaded onto a TR2 Post (Ø1/2" x 2" tall) and secured to the breadboard with a UPH2 Universal Post Holder. To attenuate the amount of light entering the Shack-Hartmann wavefront sensor, NE10A and NE20A Ø1" Mounted Neutral Density Filters, which have an optical density of 1.0 and 2.0, respectively, are used. Since the sensor itself features internal C-mount threading and the ND filter is housed inside a 0.3" long SM1 (1.035"-40) lens tube, an SM1A9 C-Mount to SM1 Adapter is necessary to mate the ND filter to the front of the WFS150-5C.

The portion of light transmitted by the beamsplitter can be blocked by a beam block (#14) that is constructed from an SM1A7 Alignment blank that has been threaded into an LMR1 Lens Mount and onto a TR3 Post. The post can be secured to the breadboard using a UPH2 Universal Post Holder. Alternatively, the beam block can be removed and the light can be launched into an application.

A Note about the Optics Included with the Adaptive Optics Kits:
The AOK1-UM01, AOK1-UP01, AOK5-UM01, and AOK5-UP01 AO Kits include the same the optical and mechanical components, with a few exceptions which are detailed in the table below. The AOK2-UM01 features a slightly different components list due to the use of the DM32-35-UM01 Mini-DM. Components included in all three kits are outlined in the table on the *Components* tab.

Figure 2. A photograph of an AOK1-UM01 Adaptive Optics kit. Please note that the breadboard is not included with the purchase of an AO kit. The key components, which will be discussed in the text below, are numbered. Click here to see the same view of the AOK2-UM01 kit.

Click to Enlarge

Click to Enlarge

Figure 3. A photograph showing an alternate view of an assembled Adaptive Optics Kit. Please note that a breadboard is not included with the AO Kit. Click here to see the same view of the AOK2-UM01 kit.

Wavelength-Dependent Components Included with Each AO Kit				
AO Kit Item #	Wavefront Sensor	Deformable Mirror	Lenses	Mirrors
AOK1-UM01	WFS150-5C	DM140A-35-UM01	LA1608-A	PF10-03-M01
AOK1-UP01	WFS150-5C	DM140A-35-UP01	LA1608-B	PF10-03-P01
AOK2-UM01	WFS150-5C	DM32-35-UM01	LA1608-A	PF10-03-M01

AOK5-UM01	WFS20-5C	DM140A-35-UM01	LA1608-A	PF10-03-M01
AOK5-UP01	WFS20-5C	DM140A-35-UP01	LA1608-B	PF10-03-P01

Hide Components

COMPONENTS

AO Kit Components								
AOK1			**AOK2-UM01**			**AOK5**		
Item #	Qty.	Photo	Item #	Qty.	Photo	Item #	Qty.	Photo
WFS150-5C CCD-Based Wavefront Sensor	1		WFS150-5C CCD-Based Wavefront Sensor	1		WFS20-5C High-Speed CMOS-Based Wavefront Sensor	1	
DM140A-35 Deformable Mirror	1		DM32-35-UM01 Deformable Mirror	1		DM140A-35 Deformable Mirror	1	
Light Source								
CPS180 Collimated Laser Module	1		CPS180 Collimated Laser Module	1		CPS180 Collimated Laser Module	1	
LDS5 5V DC Regulated Power Supply	1		LDS5 5V DC Regulated Power Supply	1		LDS5 5V DC Regulated Power Supply	1	
Optics								
AOK1			**AOK2-UM01**			**AOK5**		
LA1608-A or LA1608-B 75 mm Focal Length Plano-Convex Lens[a]	6		LA1608-B 75 mm Focal Length Plano-Convex Lens	4		LA1608-A or LA1608-B 75 mm Focal Length Plano-Convex Lens[a]	6	
			LA1433-B 150 mm Focal Length Plano-Convex Lens	2				
PF10-03-P01 Protected-Silver-Coated or PF10-03-M01 Protected-Gold-Coated Mirror[a]	2		PF10-03-M01 Protected-Gold-Coated Mirror	2		PF10-03-P01 Protected-Silver-Coated or PF10-03-M01 Protected-Gold-Coated Mirror[a]	2	
NE20A Mounted Ø1" Absorptive Neutral Density Filter	1		NE20A Mounted Ø1" Absorptive Neutral Density Filter	1		NE20A Mounted Ø1" Absorptive Neutral Density Filter	1	
NE10A Mounted Ø1" Absorptive Neutral Density Filter	1		NE10A Mounted Ø1" Absorptive Neutral Density Filter	1		NE10A Mounted Ø1" Absorptive Neutral Density Filter	1	
BP108 Pellicle Beamsplitter	1		BP108 Pellicle Beamsplitter	1		BP108 Pellicle Beamsplitter	1	
Mechanics								
AOK1			**AOK2-UM01**			**AOK5**		
KS2D Kinematic Mount	1		DM-KM1 Kinematic Mount (Sold in Kit Only)	1		KS2D Kinematic Mount	1	
KCB1 Right-Angle Kinematic 30 mm Cage Mount	2		KCB1 Right-Angle Kinematic 30 mm Cage Mount	2		KCB1 Right-Angle Kinematic 30 mm Cage Mount	2	
CXY1 30 mm Cage-Compatible XY Translation Mount	3		CXY1 30 mm Cage-Compatible XY Translation Mount	3		CXY1 30 mm Cage-Compatible XY Translation Mount	3	
CP02 Threaded 30 mm Cage Plate	4		CP02 Threaded 30 mm Cage Plate	4		CP02 Threaded 30 mm Cage Plate	4	
CP02B Cage Plate Adapter	4		CP02B Cage Plate Adapter	4		CP02B Cage Plate Adapter	4	
CB1 30 mm Cage System U-Bench	1		CB1 30 mm Cage System U-Bench	1		CB1 30 mm Cage System U-Bench	1	
LMR1 Lens Mount for Ø1" Optics	1		LMR1 Lens Mount for Ø1" Optics	1		LMR1 Lens Mount for Ø1" Optics	1	
AD11F SM1 Adapter for Ø11 mm Collimators	1		AD11F SM1 Adapter for Ø11 mm Collimators	1		AD11F SM1 Adapter for Ø11 mm Collimators	1	

AOK1	Qty	AOK2-UM01	Qty	AOK5	Qty
SM1A9 C-Mount to SM1 Adapter	1	SM1A9 C-Mount to SM1 Adapter	1	SM1A9 C-Mount to SM1 Adapter	1
KM100BP Pellicle Kinematic Mount	1	KM100BP Pellicle Kinematic Mount	1	KM100BP Pellicle Kinematic Mount	1
KM100WFS Kinematic Mount for Wavefront Sensor	1	KM100WFS Kinematic Mount for Wavefront Sensor	1	KM100WFS Kinematic Mount for Wavefront Sensor	1

AOK1	Qty	AOK2-UM01	Qty	AOK5	Qty
UPH2 2" High Universal Post Holder	10	UPH2 2" High Universal Post Holder	10	UPH2 2" High Universal Post Holder	10
TR2 Ø1/2" x 2" Post	10	TR3 Ø1/2" x 2" Post	10	TR2 Ø1/2" x 2" Post	10
ER1 Ø6 mm x 1" Cage Rod	4	ER1 Ø6 mm x 1" Cage Rod	4	ER1 Ø6 mm x 1" Cage Rod	4
ER1.5 Ø6 mm x 1.5" Cage Rod	4	ER3 Ø6 mm x 3" Cage Rod	4	ER1.5 Ø6 mm x 1.5" Cage Rod	4
ER3 Ø6 mm x 3" Cage Rod	4	ER4 Ø6 mm x 4" Cage Rod	8	ER3 Ø6 mm x 3" Cage Rod	4
ER6 Ø6 mm x 6" Cage Rod	12	ER6 Ø6 mm x 6" Cage Rod	12	ER6 Ø6 mm x 6" Cage Rod	12
ERSCA ER Rod Adapter	4	ERSCA ER Rod Adapter	4	ERSCA ER Rod Adapter	4
RS2 Ø1" x 2" Pillar Post Extention	1	TR2 Ø1/2" x 2" Post	4	RS2 Ø1" x 2" Pillar Post Extention	1
RSH2 Ø1" Post Holder with Flexure Mechanism	1	UPH1 Universal Post Holder	4	RSH2 Ø1" Post Holder with Flexure Mechanism	1
PF175 Clamping Fork for Ø1.5" Pedestal Post	1			PF175 Clamping Fork for Ø1.5" Pedestal Post	1

Alignment Tools

AOK1	Qty	AOK2-UM01	Qty	AOK5	Qty
CPA1 30 mm Cage System Alignment Plate	3	CPA1 30 mm Cage System Alignment Plate	1	CPA1 30 mm Cage System Alignment Plate	3
SM1A7 SM1 Alignment Disk	1	SM1A7 SM1 Alignment Disk	1	SM1A7 SM1 Alignment Disk	1

- Kits with an aluminum-coated Deformable Mirror contain the LA1608-A and PF10-03-P01, while kits with a gold-coated mirror include the LA1608-B and PF10-03-M01.

Hide AO Tutorial

AO TUTORIAL

Introduction:

Adaptive optics (AO) is a rapidly growing multidisciplinary field encompassing physics, chemistry, electronics, and computer science. AO systems are used to correct (shape) the wavefront of a beam of light. Historically, these systems have their roots in the international astronomy and US defense communities. Astronomers realized that if they could compensate for the aberrations caused by atmospheric turbulence, they would be able to generate high resolution astronomical images; with sharper images comes an additional gain in contrast, which is also advantageous for astronomers since it means that they can detect fainter objects that would otherwise go unnoticed. While astronomers were trying to overcome the blurring effects of atmospheric turbulence, defense contractors were interested in ensuring that photons from their high-power lasers would be correctly pointed so as to destroy strategic targets. More recently, due to advancements in the sophistication and simplicity of AO components, researchers have utilized these systems to make breakthroughs in the areas of femtosecond pulse shaping, microscopy, laser communication, vision correction, and retinal imaging. Although dramatically different fields, all of these areas benefit from an AO system due to undesirable time-varying effects.

Typically, an AO system is comprised from three components: (1) a wavefront sensor, which measures these wavefront deviations, (2) a deformable mirror, which can change shape in order to modify a highly distorted optical wavefront, and (3) real-time control software, which uses the information collected by the wavefront sensor to calculate the appropriate shape that the deformable mirror should assume in order to compensate for the distorted wavefront. Together, these three components operate in a closed-loop fashion. By this, we mean that any changes caused by the AO system can also be detected by that system. In principle, this closed-loop system is fundamentally simple; it measures the phase as a function of the position of the optical wavefront under consideration, determines its aberration, computes a correction, reshapes the deformable mirror, observes the consequence of that correction, and then repeats this process over and over again as necessary if the phase aberration varies with time. Via this procedure, the AO system is able to improve optical resolution of an image by removing aberrations from the wavefront of the light being imaged.

The Wavefront Sensor:

The role of the wavefront sensor in an adaptive optics system is to measure the wavefront deviations from a reference wavefront. There are three basic configurations of wavefront sensors available: Shack-Hartmann wavefront sensors, shearing interferometers, and curvature sensors. Each has its own advantages in terms of noise, accuracy, sensitivity, and ease of interfacing it with the control software and deformable mirror. Of these, the Shack-Hartmann wavefront sensor has been the most widely used.

A Shack-Hartmann wavefront sensor uses a lenslet array to divide an incoming beam into a bunch of smaller beams, each of which is imaged onto a CCD camera, which is placed at the focal plane of the lenslet array. If a uniform plane wave is incident on a Shack-Hartmann wavefront sensor (refer to Fig. 1), a focused spot is formed along the optical axis of each lenslet, yielding a regularly spaced grid of spots in the focal plane. However, if a distorted wavefront (i.e., any non-flat wavefront) is used, the focal spots will be displaced from the optical axis of each lenslet. The amount of shift of each spot's centroid is proportional to the local slope (i.e., tilt) of the wavefront at the location of that lenslet. The wavefront phase can then be reconstructed (within a constant) from the spot displacement information obtained (see Fig. 2).
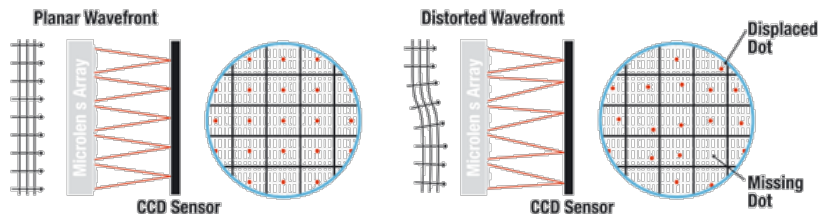

Figure 1. When a planar wavefront is incident on the Shack-Hartmann wavefront sensor's microlens array, the light imaged on the CCD sensor will display a regularly spaced grid of spots. If, however, the wavefront is aberrated, individual spots will be displaced from the optical axis of each lenslet; if the displacement is large enough, the image spot may even appear to be missing. This information is used to calculate the shape of the wavefront that was incident on the microlens array.
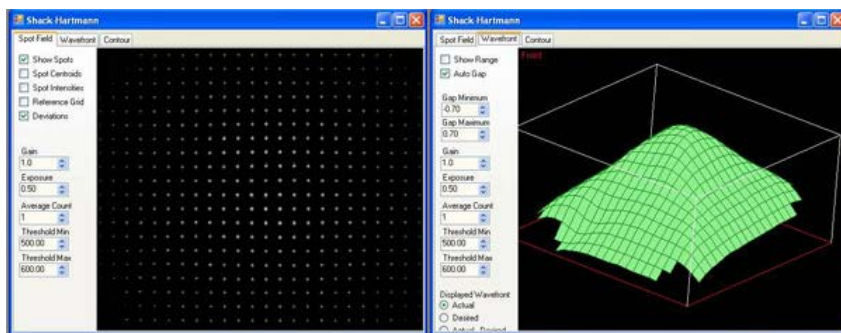

Figure 2. Two Shack-Hartmann wavefront sensor screen captures are shown: the spot field (left-hand frame) and the calculated wavefront based on that spot field information (right-hand frame).

The four parameters that greatly affect the performance of a given Shack-Hartmann wavefront sensor are the number of lenslets (or lenslet diameter, which typically ranges from ~100 – 600 μm), dynamic range, measurement sensitivity, and the focal length of the lenslet array (typical values range from a few millimeters to about 30 mm). The number of lenslets restricts the maximum number of Zernike coefficients that a reconstruction algorithm can reliably calculate; studies have found that the maximum number of coefficients that can be used to represent the original wavefront is approximately the same as the number of lenslets. When selecting the number of lenslets needed, one must take into account the amount of distortion s/he is trying to model (i.e., how many Zernike coefficients are needed to effectively represent the true wave aberration). When it comes to measurement sensitivity θ_{min} and dynamic range θ_{max}, these are competing specifications (see Fig. 3 to the right). The former determines the minimum phase that can be detected while the latter determines the maximum phase that can be measured.
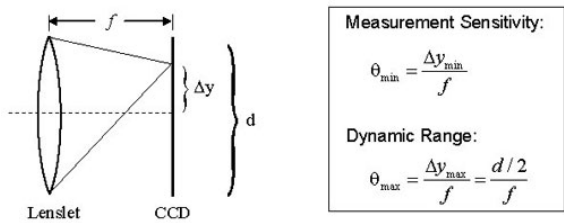

Measurement Sensitivity:

$$\theta_{min} = \frac{\Delta y_{min}}{f}$$

Dynamic Range:

$$\theta_{max} = \frac{\Delta y_{max}}{f} = \frac{d/2}{f}$$

Figure 3. Dynamic range and measurement sensitivity are competing properties of a Shack-Hartmann wavefront sensor. Here, f, Δy, and d represent the focal length of the lenslet, the spot displacement, and the lenslet diameter, respectively. The equations provided for the measurement sensitivity θ_{min} and the dynamic range θ_{max} are obtained using the small angle approximation. θ_{min} is the minimum wavefront slope that can be measured by the wavefront sensor. The minimum detectable spot displacement Δy_{min} depends on the pixel size of the photodetector, the accuracy of the centroid algorithm, and the signal to noise ratio of the sensor. θ_{max} is the maximum wavefront slope that can be measured by the wavefront sensor and corresponds to a spot displacement of Δy_{max}, which is equal to half of the lenslet diameter. Therefore, increasing the sensitivity will decrease the dynamic range and vice versa.

A Shack-Hartmann sensor's measurement accuracy (i.e., the minimum wavefront slope that can be measured reliably) depends on its ability to precisely measure the displacement of a focused spot with respect to a reference position, which is located along the optical axis of the lenslet. A conventional algorithm will fail to determine the correct centroid of a spot if it partially overlaps another spot or if the focal spot of a lenslet falls outside of the area of the sensor assigned to detect it (i.e., spot crossover). Special algorithms can be implemented to overcome these problems, but they limit the dynamic range of the sensor (i.e., the maximum wavefront slope that can be measured reliably). The dynamic range of a system can be increased by using a lenslet with either a larger diameter or a shorter focal length. However, the lenslet diameter is tied to the needed number of Zernike coefficients; therefore, the only other way to increase the dynamic range is to shorten the focal length of the lenslet, but this in turn, decreases the measurement sensitivity. Ideally, choose the longest focal length lens that meets both the dynamic range and measurement sensitivity requirements.

The Shack-Hartmann wavefront sensor is capable of providing information about the intensity profile as well as the calculated wavefront. Be careful not to confuse these. The left-hand frame of Fig. 4 shows a sample intensity profile, whereas the right-hand frame shows the corresponding wavefront profile. It is possible to obtain the same intensity profile from various wavefuncton distributions.
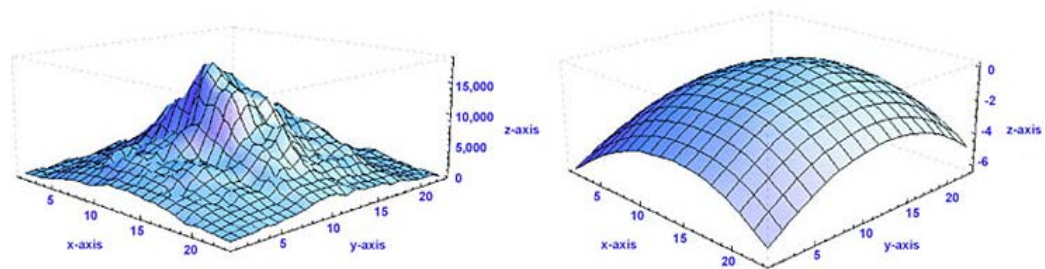

Figure 4. Several pieces of information are provided by the Shack-Hartmann wavefront sensor, including information about the total power at each lenslet and the calculated wavefront distribution present. Here, the left-hand frame shows a sample intensity profile, while the right-hand frame shows the corresponding wavefront.

The Deformable Mirror:
The deformable mirror (DM) changes shape in response to position commands in order to compensate for the aberrations measured by the Shack-Hartmann wavefront sensor (refer to the *Aberrations* tab to learn more about the aberrations that the DM can correct). Ideally, it will assume a surface shape that is conjugate to the aberration profile (see Fig. 5). In many cases, the surface profile is controlled by an underlying array of actuators that move in and out in response to an applied voltage. Deformable mirrors come in several different varieties, but the two most popular categories are segmented and continuous (see Fig. 6). Segmented mirrors are comprised from individual flat segments that can either move up and down (if each segment is controlled by just one actuator) or have tip, tilt, and piston motion (if each segment is controlled by three actuators). These mirrors are typically used in holography and for spatial light modulators. Advantages of this configuration include the ability to manufacture the segments to tight tolerances, the elimination of coupling between adjacent segments of the DM since each acts independently, and the number of degrees of freedom per segment. However, on the down side, the regularly spaced gaps between the segments act like a diffraction pattern, thereby introducing diffractive modes into the beam. In addition, segmented mirrors require more actuators than continuous mirrors to compensate for a given incoming distorted wavefront. To address the optical problems with segmented DMs, continuous faceplate DMs (such as those included in our AO Kits) were fabricated. They offer a higher fill factor (i.e., the percentage of the mirror that is actually reflective) than their segmented counterparts. However, their drawback is that the actuators are mechanically coupled. Therefore, when one actuator moves, there is some finite response along the entire surface of the mirror. The 2D shape of the surface caused by displacing one actuator is called the *influence function* for that actuator. Typically, adjacent actuators of a continuous DM are displaced by 10-20% of the actuation height; this percentage is known as the *actuator coupling*. Note that segmented DMs exhibit zero coupling but that isn't necessarily desirable.
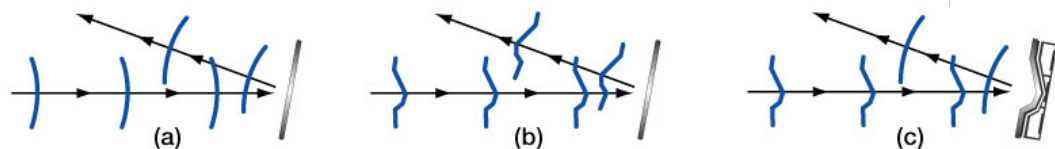

Figure 5. The aberration compensation capabilities of a flat and MEMS deformable mirror are compared. (a) If an unabberated wavefront is incident on a flat mirror surface, the reflected wavefront will remain unabberated. (b) A flat mirror is not able to compensate for any deformations in the wavefront; therefore, an incoming highly aberrated wavefront will retain its aberrations upon reflection. (c) A MEMS deformable mirror is able to modify its surface profile to compensate for aberrations; the DM assumes the appropriate conjugate shape to modify the highly aberrated incident wavefront so that it is unaberrated upon reflection.
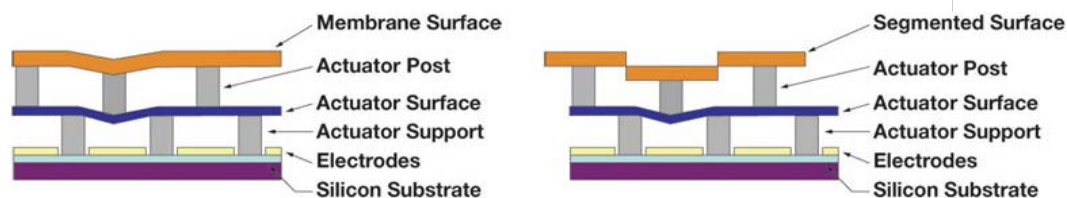

Figure 6. Cross sectional schematics of the main components of BMC's continuous (left) and segmented (right) MEMS deformable mirrors.

The range of wavefronts that can be corrected by a particular DM is limited by the actuator stroke and resolution, the number and distribution of actuators, and the model used to determine the appropriate control signals for the DM; the first two are physical limitations of the DM itself, whereas the last one is a limitation of the control software. The actuator stroke is another term for the dynamic range (i.e., the maximum displacement) of the DM actuators and is typically measured in microns. Inadequate actuator stroke leads to poor performance and can prevent the convergence of the control loop. The number of actuators determines the number of degrees of freedom that the mirror can correct for. Although many different actuator arrays have been proposed, including square, triangular, and hexagonal, most DMs are built with square actuator arrays, which are easy to position on a Cartesian coordinate system and map easily to the square detector arrays on the wavefront sensors. To fit the square array on a circular aperture, the corner actuators are sometimes removed (e.g., the deformable mirror included with the AOK1-UM01 or AOK1-UP01 has a 12 x 12 actuator configuration but only 140 actuators since the corner ones are not used). Although more actuators can be placed within a given area using some of the other configurations, the additional fabrication complexity usually does not warrant that choice.

Figure 7 (left frame) shows a screen shot of a cross formed on the 12 x 12 actuator array of the DM included with the adaptive optics kit. To create this screen shot, the voltages applied to the middle two rows and middle two columns of actuators were set to cause full deflection of the mirror membrane. In addition to the software screen shot depicting the DM

surface, quasi-dark field illumination was used to obtain a photograph of the actual DM surface when programmed to these settings (see Fig. 7, right frame)

The Control Software:
In an adaptive optics setup, the control software is the vital link between the wavefront sensor and the deformable mirror. It converts the wavefront sensor's electrical signals, which are proportional to the slope of the wavefront, into compensating voltage commands that are sent to each actuator of the DM. The closed-loop bandwidth of the adaptive optics system is directly related to the speed and accuracy with which this computation is done, but in general, these calculations must occur on a shorter time scale than the aberration fluctuations.

Figure 7. A cross-like pattern is created on the DM surface by applying the voltages necessary for maximum deflection of the 44 actuators that comprise the middle two rows and middle two columns of the array. The frame on the left shows a screen shot of the AO kit software depicting the DM surface, whereas the frame on the right, which was obtained through quasi-dark field illumination, shows the actual DM surface when programmed to these settings. Note that the white light source used for illumination is visible in the lower right-hand corner of the photograph.

In essence, the control software uses the spot field deviations to reconstructs the phase of the beam (in this case, using Zernike polynomials) and then sends conjugate commands to the DM. A least-squares fitting routine is applied to the calculated wavefront phase in order to determine the effective Zernike polynomial data outputted for the end user. Although not the only form possible, Zernike polynomials provide a unique and convenient way to describe the phase of a beam. These polynomials form an orthogonal basis set over a unit circle with different terms representing the amount of focus, tilt, astigmatism, comma, et cetera; the polynomials are normalized so that the maximum of each term (except the piston term) is +1, the minimum is –1, and the average over the surface is always zero. Furthermore, no two aberrations ever add up to a third, thereby leaving no doubt about the type of aberration that is present.
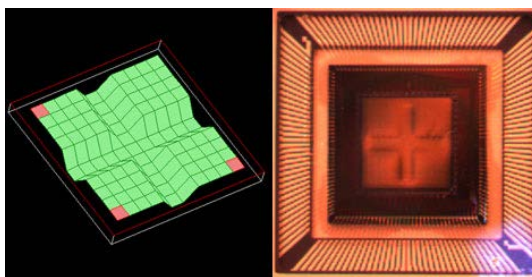
Hide Aberrations

A B E R R A T I O N S

Monochromatic Aberrations

There are five primary monochromatic aberrations, which can be further divided into two subgroups: those that deteriorate the image (spherical aberration, coma, and astigmatism) and those that deform the image (field curvature and distortion). These aberrations are a direct result of departures from first-order (i.e., $\sin\theta \approx \theta$) theory, which assumes the light rays make small angles with the principal axis. As soon as one wants to consider light rays incident on the periphery of a lens, the statement $\sin\theta \approx \theta$, which forms the basis of paraxial optics, is no longer satisfactory and one must consider more terms in the expansion:

$$\sin \theta = \theta - \frac{\theta^3}{3!} + \frac{\theta^5}{5!} - \frac{\theta^7}{7!} + \ldots$$

The five primary monochromatic aberrations were first studied by Ludwig von Seidel, and hence, they are frequently referred to as the *Seidel aberrations*. Please note that since the expansion of $\sin\theta$ is an infinite sum, the five monochromatic aberrations discussed below are not the only ones possible; there are additional higher-order aberrations that make smaller contributions to image degradation. The surface of the deformable mirror can be altered to accommodate all of these types of monochromatic aberrations.

1) Spherical Aberrations

For parallel incoming light rays, an ideal lens will be able to focus the rays to a point on the optical axis as shown in Fig. 1a; consequently, under ideal circumstances, the image of a point source that is located on the optical axis will be a bright circular disk surrounded by faint rings (see the Airy diffraction pattern shown in Fig. 1b). However, in reality, the light rays that strike a spherical converging lens far from the principal axis will be focused to a point that is closer to the lens than those light rays that strike the spherical lens near the principal axis (see Fig. 1c). Consequently, there is no single focus for a spherical lens, and the image will appear to be blurred; instead of having an Airy diffraction pattern in which nearly all the light is contained in a central bright circular spot, spherical aberration will redistribute some of the light from the central disk to the surrounding rings (see Fig. 1d), thereby reducing image contrast. Whenever spherical aberration is present, the best focus for an uncorrected lens will be somewhere between the focal planes of the peripheral and axial rays. Please note that spherical aberration only pertains to object points that are located on the optical axis.
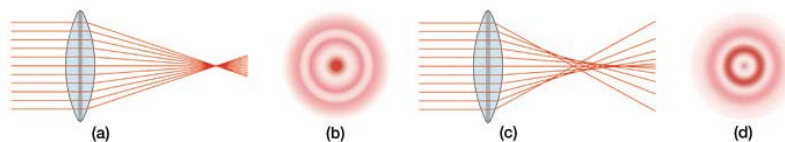

Figure 1. Comparison of an ideal situation to one in which spherical aberration is present. (a) For a perfect lens, all incoming light rays get focused to a single point. (b) The Airy diffraction pattern corresponding to a point source that has been imaged by a perfect lens consists of a bright central spot surrounded by faint concentric rings. (c) For a real lens, light incident on the edges of a lens is refracted more than the light striking the center of the lens, and thus, there is not one unique focal point for all incident light rays. (d) Spherical aberration degrades resolution by redistributing some of the light from the central bright spot to the surrounding concentric rings.

2) Coma

Coma, or comatic aberration, is an image-degrading aberration associated with object points that are even slightly off axis. When an off-axis bundle of light is incident on a lens, the light will undergo different amounts of refraction depending on where it strikes the lens (see Fig. 2a); as a result, each annulus of light will focus onto the image plane at a slightly different height and with a different spot size (see Fig. 2b), thereby leading to different transverse magnifications.

The resulting image of a point source, which is shown in Fig. 2c, is a complicated asymmetrical diffraction pattern with a bright central core and a triangular flare that departs drastically from the classical Airy pattern shown in Fig 1b above. The elongated comet-like structure from which this type of aberration takes its name can extend either towards or away from the optical axis depending on whether the comatic aberration is negative or positive, respectively. Due to the asymmetry that coma causes in images, many consider it to be the worst type of aberration.
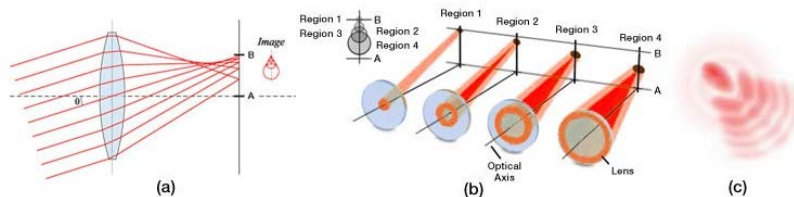

Figure 2. The effects of positive coma are shown. (a) When a light source is off-axis, the various portions of the lens do not refract the light to the same point on the image plane. (b) The central region of the lens forms a point image at the vertex of the cone, while larger rings on the periphery of the lens correspond to larger comatic circles that are displaced farther from the principal axis. (c) Coma leads to a complicated asymmetrical comet-like diffraction pattern characterized by an elongated structure of blotches and arcs. Note that the diffraction pattern shown assumes no spherical aberration.

3) Astigmatism

Astigmatism, like coma, is an aberration that arises when an object point is moved away from the optical axis. Under such conditions, the incident cone of light will strike the lens obliquely, leading to a refracted wavefront characterized by two principal curvatures that ultimately determine two different focal image points. Figure 3a shows the two planes one needs to consider: the tangential (also known as the meridional) plane and the sagittal plane; the tangential plane is defined by the chief ray (i.e., the light ray from the object that passes through the center of the lens) and the optical axis, while the sagittal plane is a plane that contains the chief ray and is perpendicular to the tangential plane. In addition to the chief light ray, Fig. 3a also shows two other off-axis light rays, one passing through the tangential plane and the other passing through the sagittal plane. For complex multi-element lens systems (e.g., microscope objective or ASOM system), the tangential plane remains coherent from one end of the system to the other while the sagittal plane usually changes slope as the chief ray's propagation direction is altered by the various components in the lens system. Consequently, in general, the focal lengths associated with these planes will be different (see Fig. 3b). If the sagittal focus and the tangential focal points are coincident, then the object point is on axis and the lens is free of astigmatism. However, as the amount of astigmatism present increases, the distance between these two foci will also increase, and as a result, the image will lose definition around its edges. The presence of astigmatism will cause the ideal circular point image to be blurred into a complicated elongated diffraction pattern that appears more linelike when more astigmatism is present (see Figs. 3c and 3d).
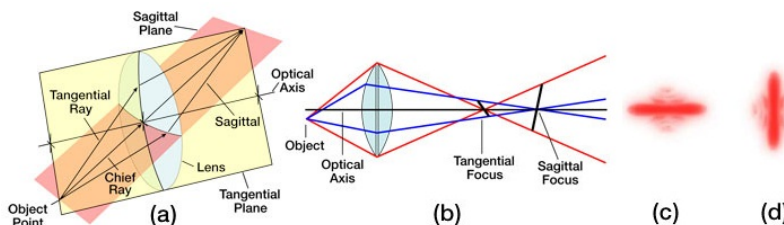

Figure 3. The effects of astigmatism, assuming the absence of spherical aberration and coma, are illustrated. (a) The tangential and sagittal planes are shown. (b) Light rays in the tangential and sagittal planes are refracted differently, ultimately leading to two different focal planes, which are labeled as the tangential focus and sagittal focus. (c) The Airy diffraction pattern of a point source as viewed at the tangential focal plane. (d) The Airy diffraction pattern of a point source as viewed at the sagittal focal plane.

4) Field Curvature

For most optical systems, the final image must be formed on a planar surface; however, in actuality, a lens that is free of all other off-axis aberrations creates an image on a curved surface known as a Petzval surface. This nominal curvature of this surface, which is known as the Petzval curvature, is the reciprocal of the lens radius. For a positive lens, this surface curves inward towards the object plane, whereas for a negative lens, the surface curves away from that plane. The field curvature aberration arises from forcing a naturally curved image surface into a flat one. For the image, the presence of field curvature makes it impossible to have both the edges and central region of the image be crisp simultaneously. If the focal plane is shifted to the vertex of the Petzval surface (Position A in Fig. 4), the central part of the image will be in focus while the outer portion of the image will be blurred, making it impossible to distinguish minor structural details in this outer region. Alternatively, if the image plane is moved to the edges of the Petzval surface (Position B in Fig. 4), the opposite effect occurs; the edges of the image will come into focus, but the central region will become blurred. The best compromise between these two extremes is to place the image plane somewhere in between the vertex and edges of the Petzval surface, but regardless of its location, the image will never appear sharp and crisp over the entire field of view.
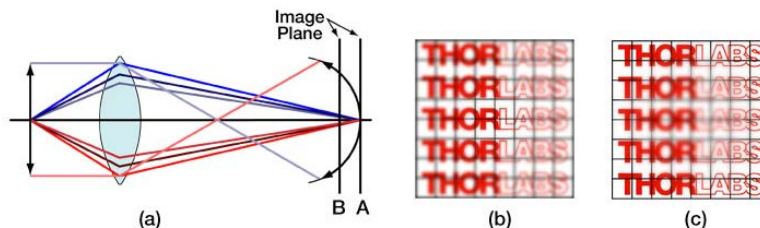

Figure 4. Field curvature, an aberration associated with off-axis objects, arises because the best image is not formed on the paraxial image plane but on a parabolic surface called the Petzval surface. (a) Depending on the location of the focal plane along the optic axis, either the central (if at location A) or peripheral (if at location B) portions of the field of view will be in focus but not both. (b) The central portion of the image will be crisp if the image plane is located at position A. (c) The edges of the image will be sharply in focus if the image plane is located at position B.

5) Distortion

The last of the Seidel aberrations is distortion, which is easily recognized in the absence of all other monochromatic aberrations because it deforms the entire image even though each point is sharply focused. Distortion arises because different areas of the lens usually have different focal lengths and magnifications. If no distortion is present in a lens system, the image will be a true magnified reproduction of the object (see Fig. 5b). However, when distortion is present, off-axis points are imaged either at a distance greater than normal or less than normal, leading to a pincushion (see Fig. 5a) or barrel (see Fig. 5c) shape, respectively.
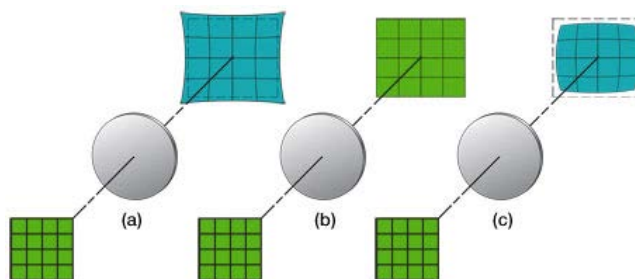
Figure 5. The effects of distortion, assuming the absence of all other forms of aberration, are illustrated. (a) Positive or pincushion distortion occurs when the transverse magnification of a lens increases with the axial distance; this effect causes each image point to be displaced radially outward from the center, with the most distant points undergoing the largest displacements. (b) If no distortion is present, the image will be a scaled duplicate of the object. (c) Negative or barrel distortion occurs when the transverse magnification of a lens decreases with axial distance; in this case, each image point moves radially inward toward the center; again, the most distant points undergo the largest displacements.

Chromatic Aberrations

The monochromatic aberrations discussed above can all be compensated for using a deformable mirror such as the one included in these adaptive optics kits. However, when a broadband light source is used, chromatic aberrations will result. Since a DM cannot compensate for these aberrations, we will only briefly mention them here. Chromatic aberrations, which come in two forms (i.e., lateral and longitudinal), arise from the variation of the index of refraction of a lens with incident wavelength. Since blue light is refracted more than red light, the lens is not capable of focusing all colors to the same focal point; therefore, the image size and focal point for each color will be slightly different, leading to an image that is surrounded by a halo. Generally, since the eye is most sensitive to the green part of the spectrum, the tendency is to focus the lens for that region; if the image plane is then moved towards (away from) the lens, the periphery of the blurred image will be tinted red (blue).

Hide Off-Axis Imaging

OFF-AXIS IMAGING

Introduction

Off-axis scanning is frequently used in many imaging techniques including Optical Coherence Tomography (OCT), Confocal Microscopy, and Adaptive Scanning Optical Microscopy (ASOM). Without adaptive optics, images obtained using these techniques will suffer from the off-axis aberrations discussed in the *Aberrations* tab, thereby requiring one to choose between resolution and field of view. However, by using a deformable mirror, this tradeoff is overcome. To learn more about how a deformable mirror works and its role in an adaptive optics system, please see the *AO Tutorial* tab.

An Example: ASOM

As an example, consider Thorlabs' Adaptive Scanning Optical Microscope (ASOM), which is shown in Fig. 1 at the right and combines a high-speed steering mirror, large aperture scan lens, and micro-electro-mechanical (MEMS) deformable mirror to provide a large field of view (Ø40 mm) while preserving resolving power (1.5 µm over the entire field of view) and a high image acquisition rate (30 fps). As the imaged area on the sample is changed (by changing the orientation of the fast steering mirror), the deformable mirror is used to correct the off-axis aberrations introduced by the scan lens, thus maintaining the diffraction-limited 1.5 µm resolution across the extended composite field of view.

Figure 1. (a) A schematic of Thorlabs' ASOM system, which consists of a custom-designed scan lens, a fast steering mirror, a 4.4 mm x 4.4 mm DM with a 12 x 12 grid of electrostatic actuators, and a CCD camera. (b) A photograph of the ASOM system.

ASOM works by taking a sequence of small spatially separated images in rapid succession and then assembling them to form a large composite image. Although mosaic construction has been used in the past to expand the field of view while preserving resolution, it necessitated the use of a moving stage. In contrast, the ASOM uses a high speed 2D mirror, a specially designed scanner lens assembly, a deformable mirror, and additional imaging optics to overcome this tradeoff.

Figure 2 shows a schematic of the ASOM scanner lens assembly (SLA). Unlike a traditional microscope objective, which must image onto a flat surface, the ASOM allows for a curved image field (i.e., the natural image field shape for a lens – refer to the Field Curvature Section under the *Aberrations* tab), thereby greatly simplifying the optical design and number of lens elements necessary. The figure shows four different scan angle positions. The blue lines represent on-axis scanning, whereas the green, red, and yellow lines correspond to various off-axis scan angles. For each scan angle illustrated, the wavefront distortion as a function of linear displacement from the central position on the image tile of the wavefront sensor is given.
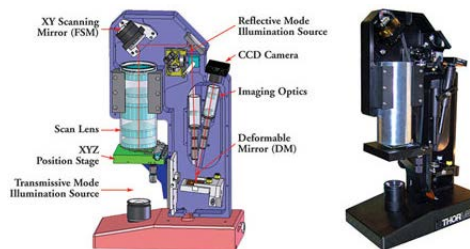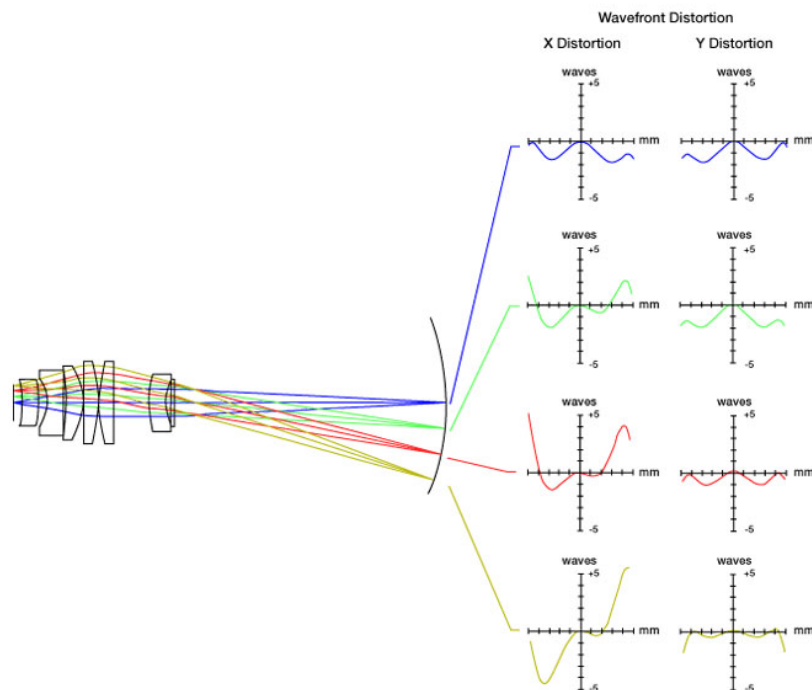
Figure 2. Adaptive Scanning Optical Microscopy (ASOM) utilizes a curved image field, thereby greatly simplifying the scanner lens assembly shown. The blue, green, red, and yellow rays represent various off-axis scan angles (0°, 2°, 4°, and 6°, respectively). For each angle, the corresponding wavefront distortion is shown. The graphs show the distortion (in waves) as a function of position on the wavefront sensor tile. Regardless of scan angle, notice that no waves of distortion are present at the exact center of each image tile. Please note that for this figure, the term "distortion" is meant to encompass all types of aberrations.

Although the large aperture scan lens and overall system layout are specifically designed to deal with field curvature, all other off-axis aberrations, such as coma and astigmatism (see the *Aberrations* tab for a detailed discussion), are still present in the ASOM system. These aberrations are compensated for at each individual field position throughout the scanner's range by a deformable mirror. Figure 3 shows the optimal DM shape for a given angular position of the high speed steering mirror.
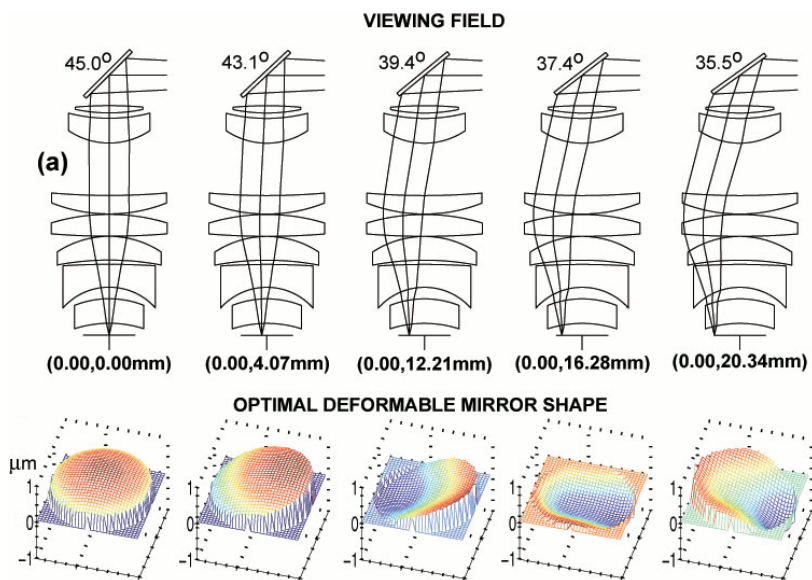

Figure 3. The angular position of the 2D steering mirror defines the observable field position. Here, the various mirror positions map out the image at five points along the y-axis. For each angular position of the high speed steering mirror shown in frame (a), the corresponding optimal deformable mirror shape is shown in frame (b). Note that the DM topology configuration necessary to correct the image at each field position is not trivial.

The deformable mirror's impressive wavefront correction abilities are demonstrated in Fig. 4, which shows an air force target imaged using a flat mirror in frame (a) and a deformable mirror in frame (b). In frame (a), the image is completely blurred, making it impossible to distinguish any structure, whereas, in frame (b), the smallest lines, which are only separated by 2 μm, are now discernable.
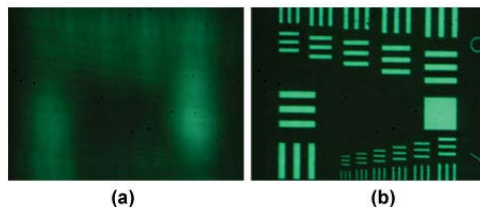

Figure 4. Resolution target imaged using (a) a flat mirror (b) an optimized deformable mirror. The smallest lines are separated by 2 μm.

[Hide Publications](#)

PUBLICATIONS

Adaptive Optics and Deformable Mirror

See also our Application Articles page, which

Publications

includes recent research using Thorlabs' Adaptive Optics equipment.

2012

Jiangpei Dou ; Deqing Ren ; Yongtian Zhu ; Xi Zhang ; Rong Li, "A dark-hole correction test for the step-transmission filter based coronagraphic system," Proc. SPIE 8442, Space Telescopes and Instrumentation 2012: Optical, Infrared, and Millimeter Wave, 84420D (September 21, 2012); doi:10.1117/12.924248.

R. Davies, M. Kasper, "Adaptive Optics for Astronomy," arXiv:1201.5741v1 [astro-ph.IM].

Wei Sun, Yang Lu, Thomas G. Bifano, Jason B. Stewart, and Charles P. Lin, "Critical considerations of pupil alignment to achieve open-loop control of MEMS deformable mirror in nonlinear laser scanning fluorescence microscopy," Proc. SPIE 8253, 82530H (2012); http://dx.doi.org/10.1117/12.909652.

Alexis Hill ; Steven Cornelissen ; Daren Dillon ; Charlie Lam ; Dave Palmer ; Les Saddlemyer, "Flexure mount for a MEMS deformable mirror for the Gemini Planet Imager," Proc. SPIE 8450, Modern Technologies in Space- and Ground-based Telescopes and Instrumentation II, 84500H (September 13, 2012); doi:10.1117/12.926842.

Katie M. Morzinski, Andrew P. Norton, Julia Wilhelmson Evans, Layra Reza, Scott A. Severson, Daren Dillon, Marc Reinig, Donald T. Gavel, Steven Cornelissen, Bruce A. Macintosh, Claire E. Max, "MEMS practice, from the lab to the telescope," arXiv:1202.1566v1 [astro-ph.IM].

Thomas Bifano, Yang Lu, Christopher Stockbridge, Aaron Berliner, John Moore, Richard Paxman, Santosh Tripathi and Kimani Toussaint, "MEMS spatial light modulators for controlled optical transmission through nearly opaque materials," Proc. SPIE 8253, 82530L (2012); http://dx.doi.org/10.1117/12.911384.

Ravi S. Jonnal, Omer P. Kocaoglu, Qiang Wang, Sangyeol Lee, and Donald T. Miller, "Phase-sensitive imaging of the outer retina using optical coherence tomography and adaptive optics," Biomedical Optics Express, Vol. 3, Issue 1, pp. 104-124 (2012) http://dx.doi.org/10.1364/BOE.3.000104.

Yiin Kuen Fuh, Kuo Chan Hsu, and Jia Ren Fan, "Rapid in-process measurement of surface roughness using adaptive optics," Optics Letters, Vol. 37, Issue 5, pp. 848-850 (2012) http://dx.doi.org/10.1364/OL.37.000848.

C. Baranec, R. Riddle, A. N. Ramaprakash, N. Law, S. Tendulkar, S. Kulkarni, R. Dekany, K. Bui, J. Davis, M. Burse, H. Das, S. Hildebrandt, S. Punnadi, R. Smith, "Robo-AO: autonomous and replicable laser-adaptive-optics and science system," Proc. SPIE 8447, Adaptive Optics Systems III, 844704 (September 13, 2012).

Renate Kupke ; Donald Gavel ; Constance Roskosi ; Gerald Cabak ; David Cowley ; Daren Dillon ; Elinor L. Gates ; Rosalie McGurk ; Andrew Norton ; Michael Peck ; Christopher Ratliff ; Marco Reinig, "ShaneAO: an enhanced adaptive optics and IR imaging system for the Lick Observatory 3-meter telescope," SPIE doi:10.1117/12.926470.

N. Jeremy Kasdin and Tyler D. Groff, "Shaped pupils with two micromechanical deformable mirrors for exoplanet imaging," 2 February 2012, SPIE Newsroom. DOI: 10.1117/2.1201201.004084.

Y. Lua, E. Ramsayb, C.R. Stockbridgea, A. Yurtc, F.H. Köklüd, T.G. Bifanoa, e, M.S. Ünlüd, e, B.B. Goldbergb, e, "Spherical aberration correction in aplanatic solid immersion lens imaging using a MEMS deformable mirror," Microelectronics Reliability Volume 52, Issues 9.10, September-October 2012.

Weiyao Zou and Stephen A. Burns, "Testing of Lagrange multiplier damped least-squares control algorithm for woofer-tweeter adaptive optics," Applied Optics, Vol. 51, Issue 9, pp. 1198-1208 (2012) http://dx.doi.org/10.1364/AO.51.001198.

Toco Y. P. Chui, Dean A. VanNasdale, and Stephen A. Burns, "The use of forward scatter to improve retinal vascular imaging with an adaptive optics scanning laser ophthalmoscope," Biomedical Optics Express, Vol. 3, Issue 10, pp. 2537-2549 (2012).

2011

K. Enya, L. Abe, S. Takeuchi, T. Kotani, T. Yamamuro, "A high dynamic-range instrument for SPICA for coronagraphic observation of exoplanets and monitoring of transiting exoplanets," arXiv:1110.2621v1 [astro-ph.IM].

M. B. Roopashree, Akondi Vyas, and B. Raghavendra Prasad, "A novel model of influence function: calibration of a continuous membrane deformable mirror," Proc. of Int. Conf. on Advances in Electrical & Electronics 2011 ACEEE DOI: 02.AEE.2011.02.49.

S. Burns, W. Zou, Z. Zhong, G. Huang, and X. Qi, "Adapting AO systems for clinical Imaging," Adaptive Optics: Methods, Analysis and Applications, OSA Technical Digest (CD) (Optical Society of America, 2011), paper AMA1.

Xiaodong Tao, Bautista Fernandez, Diana C. Chen, Oscar Azucena, Min Fu, Yi Zuo and Joel Kubby, "Adaptive Optics Confocal Fluorescence Microscopy with Direct Wavefront Sensing for Brain Tissue Imaging," Proceedings of the SPIE, Volume 7931, pp. 79310L-79310L-8 (2011). DOI: 10.1117/12.876524.

Xiaodong Tao, Bautista Fernandez, Oscar Azucena, Min Fu, Denise Garcia, Yi Zuo, Diana C. Chen, and Joel Kubby, "Adaptive optics confocal microscopy using direct wavefront sensing," Optics Letters, Vol. 36, Issue 7, pp. 1062-1064 (2011).

Xiaodong Tao, Bautista Fernandez, Oscar Azucena, Min Fu, Denise Garcia, Yi Zuo, Diana C. Chen, and Joel Kubby, "Adaptive optics confocal microscopy using direct wavefront sensing," Optics Letters, Vol. 36, Issue 7, pp. 1062-1064 (2011).

Xiaodong Tao, Oscar Azucena, Min Fu, Yi Zuo, Diana C. Chen, and Joel Kubby, "Adaptive optics microscopy with direct wavefront sensing using fluorescent protein guide stars," Optics Letters, Vol. 36, Issue 17, pp. 3389-3391 (2011).

Yaopeng Zhou, Thomas Bifano and Charles Lin, "Adaptive optics two-photon fluorescence microscopy," Proc. SPIE 7931, 79310H (2011); doi:10.1117/12.875596.

Oscar Azucena, Xiaodong Tao, Justin Crest, Shaila Kotadia, William Sullivan, Donald Gavel, Marc Reinig, Scot Olivier, Joel Kubby, "Adaptive optics widefield microscope corrections using a MEMS DM and Shack-Hartmann wavefront sensor," Proc. of SPIE Vol. 7931, 79310J (2011) doi:10.1117/12.876439.

Oscar Azucena, Justin Crest, Shaila Kotadia, William Sullivan, Xiaodong Tao, Marc Reinig, Donald Gavel, Scot Olivier, and Joel Kubby, "Adaptive optics wide-field microscopy using direct wavefront sensing," Opt. Lett. 36, 825-827 (2011).

Toco Y. P. Chui, James D. Akula, Anne B. Fulton, Jennifer L. Norris, Alfredo Dubra, Melanie Campbell, Daniel X. Hammer, R. D. Ferguson, Mircea Mujat, David P. Biss, Nicusor V. Iftimia, Ankit H. Patel, and Emily Plumb, "Advanced capabilities of the multimodal adaptive optics imager," Proc. SPIE 7885, 78850A (2011).

M N Horenstein, J B Stewart, S Cornelissen, R Sumner, D S Freedman, M Datta, N Kani, P Miller, "Advanced MEMS systems for optical communication and imaging," M N Horenstein et al 2011 Journal of Physics: Conf. Ser. 301 (2011) 012056.

Akondi Vyas, M. B. Roopashree and B. Raghavendra Prasad, "Advanced Methods for Improving the Efficiency of a Shack Hartmann Wavefront Sensor," Indian Institute of Astrophysics, Koramangala, Bangalore, India.

Hao Ren, Fenggang Tao, Weimin Wang, and Jun Yao, "An out-of-plane electrostatic actuator based on the lever principle," J. Micromech. Microeng. 21 045019 doi:10.1088/0960-1317/21/4/045019.

Juan M. Bueno, Anastasia Giakoumaki, Emilio J. Gualda, Frank Schaeffel, and Pablo Artal, "Analysis of corneal stroma organization with wavefront optimized nonlinear microscopy," Cornea: June 2011 - Volume 30 - Issue 6 - pp 692-701 doi: 10.1097/ICO.0b013e3182000f94.

Diego Rativa, Brian Vohnsen, "Analysis of individual cone-photoreceptor directionality using scanning laser ophthalmoscopy," Biomedical Optics Express, Vol. 2, Issue 6, pp. 1423-1431 (2011).

Juan M. Bueno, Anastasia Giakoumaki, Emilio J. Gualda, Frank Schaeffel, and Pablo Artal, "Analysis of the chicken retina with an adaptive optics multiphoton microscope," Biomedical Optics Express, Vol. 2, Issue 6, pp. 1637-1648 (2011).

Donald Gavel, "ASTRONOMICAL IMAGING: New adaptive optics system at Lick Observatory uses MEMS," Laser Focus World, 08/01/2011.

B.B. Goldberg, A. Yurt, Y. Lu, E. Ramsay, F.H. Koklu, J. Mertz, T.G. Bifano, M.S. Unlud, "Chromatic and spherical aberration correction for silicon aplanatic solid immersion lens for fault isolation and photon emission microscopy of integrated circuits," Science Direct, http://dx.doi.org/10.1016/j.microrel.2011.07.047.

F. Kong, N. V. Proscia, K. K. Lee, and Y. Chen, "Controlling Spatial Coherence in Multimode Fibers," in Adaptive Optics: Methods, Analysis and Applications, OSA Technical Digest (CD) (Optical Society of America, 2011), paper AMC4.

Donald T. Gavel, "Development of an enhanced adaptive optics system for the Lick Observatory Shane 3-meter Telescope," Proc. SPIE 7931, 793103 (2011); http://dx.doi.org/10.1117/12.876413.

Célia Blain, Olivier Guyon, Colin Bradley, and Olivier Lardiere, "Fast iterative algorithm (FIA) for controlling MEMS deformable mirrors: principle and laboratory demonstration," Optics Express, Vol. 19, Issue 22, pp. 21271-21294 (2011) http://dx.doi.org/10.1364/OE.19.021271.

Emilio J. Gualda, Javier R. Vázquez de Aldana, M. Carmen Martínez-García, Pablo Moreno, Juan Hernández-Toro, Luis Roso, Pablo Artal, and Juan M. Bueno, "Femtosecond infrared intrastromal ablation and backscattering-mode adaptive-optics multiphoton microscopy in chicken corneas," Biomedical Optics Express, Vol. 2, Issue 11, pp. 2950-2960 (2011).

Geoff Anderson and Fassil Ghebremichael, "Holographic Adaptive Laser Optics System," .

Omer P. Kocaoglu, Sangyeol Lee, Ravi S. Jonnal, Qiang Wang, Ashley E. Herde, Jack C. Derby, Weihua Gao, and Donald T. Miller, "Imaging cone photoreceptors in three dimensions and in time using ultrahigh resolution optical coherence tomography with adaptive optics," Biomedical Optics Express, Vol. 2, Issue 4, pp. 748-763 (2011) http://dx.doi.org/10.1364/BOE.2.000748.

Lisa A. Poyneer, "Imaging extra-solar planets with adaptive optics and a MEMS mirror," SPIE Newsroom. DOI: 10.1117/2.1201102.003471.

Qiang Wang, Omer P. Kocaoglu, Barry Cense, Jeremy Bruestle, Ravi S. Jonnal, Weihua Gao, Donald T. Miller, "Imaging Retinal Capillaries Using Ultrahigh-Resolution Optical Coherence Tomography and Adaptive Optics," Invest. Ophthalmol. Vis. Sci. January 18, 2011 iovs.10-6424.

Omer P. Kocaoglu, Barry Cense, Ravi S. Jonnal, Qiang Wang, Sangyeol Lee, Weihua Gao, and Donald T. Miller, "Imaging retinal nerve fiber bundles using optical coherence tomography with adaptive optics," Vision Research, doi:10.1016/j.visres.2011.06.013.

J.M. Girkin, "Implementation of adaptive optics in beam scanning and wide-field optical microscopy," Proc. SPIE 7931, 79310E (2011).

Weiyao Zou, Xiaofeng Qi, Gang Huang, and Stephen A. Burns, "Improving wavefront boundary condition for in vivo high resolution adaptive optics ophthalmic imaging," Biomedical Optics Express, Vol. 2, Issue 12, pp. 3309-3320 (2011).

Yiin Kuen Fuh, Kuo Chan Hsu, Jia Ren Fan, Ming Xien Lin, "Induced aberrations by combinative convex/concave interfaces of refractive-index-mismatch and capability of adaptive optics correction," Microw. Opt. Technol. Lett., 53: 2610-2615. doi: 10.1002/mop.26323.

Akondi Vyas, M. B. Roopshree, B. Raghavendra Prasad, "Intensity Weighted Noise Reduction in MEMS Based Deformable Mirror Images," AIP Conf. Proc. 1391, pp. 347-349; doi:10.1063/1.3643545.

Joseph Carroll, Michael Pircher, and Robert J. Zawadzki, "Introduction: Feature Issue on Cellular Imaging of the Retina," Biomedical Optics Express, Vol. 2, Issue 6, pp. 1778-1780 (2011).

P. Martinez, E. Aller Carpentier, M. Kasper, A. Boccaletti, C. Dorrer, J. Baudrand, "Laboratory comparison of coronagraphic concepts under dynamical seeing and high-order adaptive optics correction," The Authors Monthly Notices of the Royal Astronomical Society 2011 DOI: 10.1111/j.1365-2966.2011.18529.x.

Carrasco-Casado, A.; Vergaz, R.; Sanchez-Pena, J.M.; Oton, E.; Geday, M.A.; Oton, J.M.;, "Low-Impact Air-to-Ground Free-Space Optical Communication System Design and First Results," Proc. Space Optical Systems and Applications (ICSOS), 2011 International Conference (2011).

I. Dobrev, Marc Balboa, Ryan Fossett, C. Furlong, and E. J. Harrington, "MEMS for real-time infrared imaging," MEMS and Nanotechnology, Volume 4. Proceedings of the 2011 Annual Conference on Experimental and Applied Mechanics.

Juan M. Bueno, Emilio J. Gualda, Anastasia Giakoumaki, Pablo Pérez-Merino, Susana Marcos and Pablo Artal, "Multiphoton Microscopy of Ex Vivo Corneas after Collagen Cross-Linking," Invest. Ophthalmol. Vis. Sci. July 18, 2011 vol. 52 no. 8 5325-5331 doi: 10.1167/iovs.11-7184.

Donald T. Gavel, "New adaptive-optics technology for ground-based astronomical telescopes," SPIE Newsroom. DOI: 10.1117/2.1201101.003434.

P.R. Lawson, O.P. Lay, S.R. Martin, R.D. Peters, A.J. Booth, R.O. Gappinger, A. Ksendzov and D.P. Scharf, "New technologies for exoplanet detection with mid-IR interferometers," Research, Science and Technology of Brown Dwarfs and Exoplanets: Proceedings of an International Conference held in Shangai on Occasion of a Total Eclipse of the Sun.

David Merino, Jacque L. Duncan, Pavan Tiruveedhula, and Austin Roorda, "Observation of cone and rod photoreceptors in normal subjects and patients using a new generation adaptive optics scanning laser ophthalmoscope," Biomedical Optics Express, Vol. 2, Issue 8, pp. 2189-2201 (2011).

Laurent Pueyo, Jason Kay, N. Jeremy Kasdin, Tyler Groff, Michael McElwain, Amir Giveon, and Ruslan Belikov, "Optimal dark hole generation via two deformable mirrors with stroke minimization," Applied Optics, Vol. 48, Issue 32, pp. 6296-6312.

JS Werner, JL Keltner, RJ Zawadzki, and SS Choi, "Outer retinal abnormalities associated with inner retinal pathology in nonglaucomatous and glaucomatous optic neuropathies," Cambridge Ophthalmological Symposium, Eye 25, 279-289 (March 2011).

Z. Liu, O. P. Kocaoglu, R. S. Jonnal, Q. Wang, and D. T. Miller, "Performance of an off-axis ophthalmic adaptive optics system with toroidal mirrors," Adaptive Optics: Methods, Analysis and Applications, OSA Technical Digest (CD) (Optical Society of America, 2011), paper AMA4.

Ravi S. Jonnal, Omer P. Kocaoglu, Qiang Wang, Sangyeol Lee, and Donald T. Miller, "Phase-sensitive imaging of the outer retina using optical coherence tomography and adaptive optics," Biomedical Optics Express, Vol. 3, Issue 1, pp. 104-124 (2012).

Fanting Kong, Ronald H. Silverman, Liping Liu, Parag V. Chitnis, Kotik K. Lee, and Y. C. Chen, "Photoacoustic-guided convergence of light through optically diffusive media," Optics Letters, Vol. 36, Issue 11, pp. 2053-2055 (2011).

Sotaro Ooto, MD; Masanori Hangai, MD; Nagahisa Yoshimura, MD, "Photoreceptor Restoration in Unilateral Acute Idiopathic Maculopathy on Adaptive Optics Scanning Laser Ophthalmoscopy," Archives of Opthalmology, Vol. 129 No. 12, December 2011.

Yang Lu, Samuel M. Hoffman, Christopher R. Stockbridge, Andrew P. LeGendre, Jason B. Stewart, and Thomas G. Bifano, "Polymorphic optical zoom with MEMS DMs," Proc. of SPIE Vol. 7931 79310D-1: DOI: 10.1117/12.874207.

Kevin M. Ivers, Chaohong Li, Nimesh Patel, Nripun Sredar, Xunda Luo, Hope Queener, Ronald S. Harwerth, Jason Porter, "Reproducibility of measuring lamina cribrosa pore geometry in human and non-human primates using in vivo adaptive optics imaging," Invest. Ophthalmol. Vis. Sci. May 5, 2011 iovs.11-7347.

Kevin M. Ivers, Chaohong Li, Nimesh Patel, Nripun Sredar, Xunda Luo, Hope Queener, Ronald S. Harwerth and Jason Porter, "Reproducibility of Measuring Lamina Cribrosa Pore Geometry in Human and Nonhuman Primates with In Vivo Adaptive Optics Imaging," Invest. Ophthalmol. Vis. Sci. July 2011 vol. 52 no. 8 5473-5480.

Allyson L. Hartzell, Mark G. da Silva, Herbert R. Shea, "Root Cause and Failure Analysis," MEMS Reliability, MEMS Reference Shelf, 2011, 179-214.

Yiin-Kuen Fuh, Kuo Chan Hsu, Jia Ren Fan, "Roughness measurement of metals using a modified binary speckle image and adaptive optics," Optics and Lasers in Engineering: Volume 50, Issue 3, March 2012, Pages 312-316.

J.F. Morizur, S. Armstrong, N. Treps, J. Janousek, H.A. Bachor, "Spatial reshaping of a squeezed state of light," The European Physical Journal D - Atomic, Molecular, Optical and Plasma Physics, Volume 61, Number 1, 237-239.

Toco Y.P. Chui, , Zhangyi Zhong, Stephen A. Burns, "The relationship between peripapillary crescent and axial length: Implications for differential eye growth," Science Direct, http://dx.doi.org/10.1016/j.visres.2011.08.008.

K. Enya, T. Kotani, K. Haze, K. Aono, T. Nakagawa, H. Matsuhara, H. Kataza, T. Wada, M. Kawada, K. Fujiwara, M. Mita, S. Takeuchi, K. Komatsu, S. Sakai, H. Uchida, S. Mitani, T. Yamawaki, T. Miyata, S. Sako, T. Nakamura, K. Asano, T. Yamashita, N. Narita, "The SPICA coronagraphic instrument (SCI) for the study of exoplanets," Advances in Space Research, Volume 48, Issue 2, 15 July 2011, Pages 323-333.

Lisa A. Poyneer, Brian Bauman, Steven Jones, Bruce A. Macintosh, Steven Cornelissen, Joshua Isaacs, David W. Palmer, "The use of a high-order MEMS deformable mirror in the Gemini Planet Imager," Proc. SPIE 7931, 793104 (2011).

Mark N. Horenstein, Robert Sumner, Preston Miller, Thomas Bifano, Jason Stewart, Steven Cornelissen, "Ultra-low-power multiplexed electronic driver for high resolution deformable mirror systems," Proc. SPIE 7930, 79300M (2011); http://dx.doi.org/10.1117/12.876404.

Brian Vohnsen, Diego Rativa, "Ultrasmall spot size scanning laser ophthalmoscopy," Biomedical Optics Express, Vol. 2, Issue 6, pp. 1597-1609 (2011).

Hongxin Song, Toco Yuen Ping Chui, Zhangyi Zhong, Ann E. Elsner, Stephen A. Burns, "Variation of Cone Photoreceptor Packing Density with Retinal Eccentricity and Age," Association for Research in Vision and Ophthalmology (2011).

Oscar Azucena, Justin Crest, Jian Cao, William Sullivan, Peter Kner, Donald Gavel, Daren Dillon, Scot Olivier, and Joel Kubby, "Wavefront aberration measurements and corrections through thick tissue using fluorescent microsphere reference beacons," Optics Express, Vol. 18, Issue 16, pp. 17521-17532 (2010).

Heidi Hofer, Nripun Sredar, Hope Queener, Chaohong Li, and Jason Porter, "Wavefront sensorless adaptive optics ophthalmoscopy in the human eye," Optics Express, Vol. 19, Issue 15, pp. 14160-14171 (2011).

Weiyao Zou, Xiaofeng Qi, and Stephen A. Burns, "Woofer-tweeter adaptive optics scanning laser ophthalmoscopic imaging based on Lagrange-multiplier damped least-squares algorithm," Biomedical Optics Express, Vol. 2, Issue 7, pp. 1986-2004 (2011).

P. Martinez, E. Aller Carpentier, and M. Kasper, "XAO coronagraphy with the High-Order Test bench," EPJ Web of Conferences 16, 03005 (2011).

2010

Julie Smith, "An Experimental Study Showing the Effects on a Standard PI Controller Using a Segmented MEMS DM Acting as a MOD (lambdal) Device," Proc. SPIE 7816, 78160H (2010).

Dani Guzman, Francisco Javier De Cos Juez, Richard M. Myers, Fernando Sanchez Lasheras, Laura K. Young, and Andrés Guesalaga, "Deformable mirror models for open-loop adaptive optics using non-parametric estimation techniques," Proc. SPIE Vol. **7736**

S. A. Burns, "Designing AO Retinal Imaging Systems for Real World Uses: Issues and Limitations," Frontiers in Optics, OSA Technical Digest (CD) (Optical Society of America, 2010), paper FTuB2..

Steven Cornelissen, Jason Stewart, Tom Bifano, "High Actuator Count MEMS Deformable Mirrors for Space Telescopes," Presented at Mirror Technology Days, Boulder, Colorado, USA, 7-9 June 2010.

Andrew Norton, Donald Gavel, Daren Dillon, and Steven Cornelissen, "High-power visible-laser effect on a Boston Micromachines' MEMS deformable mirror," Proc. SPIE Vol. 7736.

Scot S. Olivier, Thomas G. Bifano, and Joel A. Kubby, "Low power MEMS modulation retroreflectors for optical communication," Proc. SPIE 7595, 759505 (2010).

T. Bifano, S. Cornelissen, and P. Bierden, "MEMS deformable mirrors in astronomical adaptive optics," 1st AO4ELT conference, 06003 (2010).

Robert D. Peters, Oliver P. Lay, and Peter R. Lawson, "Mid-Infrared Adaptive Nulling for the Detection of Earth-like Exoplanets," Publications of the Astronomical Society of the Pacific (2010) Volume: 122, Issue: 887, Pages: 85-92.

Dani Guzman, Francisco Javier de Cos Juez, Richard Myers, Andrés Guesalaga, and Fernando Sánchez Lasheras, "Modeling a MEMS deformable mirror using non-parametric estimation techniques," Optics Express, Vol. 18, Issue 20, pp. 21356-21369 (2010).

C. Vogel, G. Tyler, Y. Lu, T. Bifano, R. Conan, and C. Blain, "Modeling and parameter estimation for point-actuated continuous-facesheet deformable mirrors," J. Opt. Soc. Am. A 27, A56-A63 (2010).

Curtis R. Vogel, Glenn A. Tyler, and Yang Lu, "Modeling, parameter estimation, and open-loop control of MEMS deformable mirrors," Proc. SPIE 7595, 75950E (2010). s>

Alioune Diouf, Thomas G. Bifano, Andrew P. Legendre, and Yang Lu, "Open loop control on large stroke MEMS deformable mirrors," Proc. SPIE 7595, 75950D (2010).

Katie Morzinski, Luke C. Johnson, Donald T. Gavel, Bryant Grigsby, Daren Dillon, Marc Reinig, and Bruce A. Macintosh, "Performance of MEMS-based visible-light adaptive optics at Lick Observatory: Closed- and open-loop control," Proc. SPIE 7736, 77361O (2010).

Donald T. Gavel, "Progress update on the visible light laser guidestar experiments at Lick Observatory," Proc. SPIE 7595, 759508 (2010).

Marc Reinig, Donald Gavel, Ehsan Ardestani, and Jose Renau, "Real-time control for Keck Observatory next-generation adaptive optics," Proc. SPIE 7736, 77363J (2010).

Marc Reinig, Donald Gavel, Ehsan Ardestani, and Jose Renau, "Real-time control for Keck Observatory next-generation adaptive optics," Proc. SPIE 7736, 77363J (2010).

Thomas Bifano, Steven Cornelissen, and Paul Bierden, "Recent Advances in high-resolution MEMS DM fabrication and intergration," Advanced Maui Optical and Space Surveillance Technologies Conference, 14-17 Sep 2010, Maui, HI.

Allyson L. Hartzell, Steven A. Cornelissen, Paul A. Bierden, Charlie V. Lam, and Daniel F. Davis, "Reliability of MEMS deformable mirror technology used in adaptive optics imaging systems," Proc. SPIE 7595, 75950B (2010).

Thomas Bifano, "Shaping light: MOEMS deformable mirrors for microscopes and telescopes," Proc. SPIE Vol. **7595**

Keigo Enya, "SPICA infrared coronagraph for the direct observation of exo-planets," Advances in Space Research Volume 45, Issue 8, 15 April 2010, Pages 979-999. lwr

Alioune Diouf, Thomas G. Bifano, Jason B. Stewart, Steven Cornelissen, and Paul Bierden, "Through-wafer interconnects for high degree of freedom MEMS deformable mirrors," Proc. SPIE 7595, 75950N (2010).

2009

Andrew Norton, Julia W. Evans, Donald Gavel, Daren Dillon, David Palmer and Bruce Macintosh, Katie Morzinski, and Steven Cornelissen, "Preliminary characterization of Boston Micromachines' 4096-actuator deformable mirror" Proc. SPIE, Vol. **7209**

Steven A. Cornelissen, Paul A. Bierden, Thomas G. Bifano, Charlie V. Lam, "4096-element continuous face-sheet MEMS deformable mirror for high-contrast imaging" J. Micro/Nanolith. MEMS MOEMS, Vol. **8**, 031308

Marie Levine and Rémi Soummer, "Overview of Technologies for Direct Optical Imaging of Exoplanets" NASA, JPL

Kevin L. Baker, Eddy A. Stappaerts, Doug C. Homoelle, Mark A. Henesian, Erlan S. Bliss, Craig W. Siders, and Chris P. J. Barty, "Interferometric adaptive optics for high-power laser pointing and wavefront control and phasing" J. Micro/Nanolith. MEMS MOEMS, Vol. **8**, 033040

Byung-Wook Yoo, Jae-Hyoung Park, I. H. Park, Jik Lee, Minsoo Kim, Joo-Young Jin, Jin-A Jeon, Sug-Whan Kim, and Yong-Kweon Kim, "MEMS micromirror characterization in space environments" Optics Express, Vol. 17, Issue 5, pp. 3370-3380

Sandrine Thomas, Julia W. Evans, Donald Gavel, Daren Dillon, and Bruce Macintosh, "Amplitude variations on a MEMS-based extreme adaptive optics coronagraph testbed" Applied Optics, Vol. 48, Issue 21, pp. 4077-4089

K. Enya, T. Kotani, T. Nakagawa, H. Kataza, K. Haze, S. Higuchi, T. Miyata, S. Sako, T. Nakamura, T. Yamashita, N. Narita, M. Tamura, J. Nishikawa, H. Hayano, S. Oya, Y. Itoh, M. Fukagawa, H. Shibai, M. Honda, N. Baba, N. Murakami, M. Takami, T. Matsuo, S. Ida, L. Abe, O. Guyon, M. Venet, T. Yamamuro, P. Bierden and SPICA coronagraph team, "SPICA Coronagraph Instrument (SCI) for the Direct Imaging and Spectroscopy of Exo-Planets" SPICA Workshop, 01004 (2009) DOI: 10.1051/spica/200901004

Julia W. Evans, Robert J. Zawadzki, Steve Jones, Scot Olivier and John S. Werner, "Performance of a MEMS-based AO-OCT system using Fourier reconstruction" Proc. SPIE, Vol. 7209, 720905 (2009); doi:10.1117/12.808002

Choi, Philip I.; Horn, R. B.; Rudy, A. R.; Gurman, Z. R.; Beeler, D. J.; Penprase, B. E.; Esin, A. A.; Zook, A. C. "CUCAO-Cam: The Claremont Undergraduate Colleges Adaptive Optics Camera" American Astronomical Society, AAS Meeting #214, #409.17; Bulletin of the American Astronomical Society, Vol. 41, p.674

Jason D. Kaya, Laurent A. Pueyob, and N. Jeremy Kasdin, "Demonstration of a symmetric dark hole with a stroke-minimizing correction algorithm" Proc. SPIE, Vol. **7209**, 72090G (2009); doi:10.1117/12.809815

Weiyao Zou and Stephen A. Burns, "High-accuracy wavefront control for retinal imaging with Adaptive-Influence-Matrix Adaptive Optics" Optics Express, Vol. 17, Issue 22, pp. 20167-20177

Belikov, Rusian; Angel, Roger; Bekele, Asfaw; Cahoy, Kerri; Connelley, Michael; Dettmann, Lee; Gavel, Donald; Give'on, Amir; Guyon, Olivier; Jay, Daniel; Kasdin, N. Jeremy; Kendrick, Rick; Kern, Brian; Levine, Marie; Lynch, Dana; McKelvey, Mark; Peters, Bridget; Pluznik, Eugene; Shaklan, Stueart; Shao, Michael; Sylvester, Clay; Traub, Wesley; Trauger, John; Vanderbei, Robert; Witteborn, Fred; Woodruff, Robert, "Overview of Technology Development for the Phase-Induced Amplitude Apodization (PIAA) Coronagraph" Astro2010: The Astronomy and Astrophysics Decadal Survey, Technology Development Papers, no. 38

Ying Geng, Kenneth P. Greenberg, Robert Wolfe, Daniel C. Gray, Jennifer J. Hunter, Alfredo Dubra, John G. Flannery, David R. Williams, and Jason Porter,"In Vivo Imaging of Microscopic Structures in the Rat Retina" Investigative Ophthalmology and Visual Science. 2009;50:5872-5879

Chaohong Li, Nripun Sredar, Hope Queener, Kevin Ivers and Jason Porter, "Direct slope reconstruction algorithm for woofer-tweeter adaptive optics systems" Optical Society of America, 2009

Lawrence C Sincich, Yuhua Zhang, Pavan Tiruveedhula, Jonathan C Horton & Austin Roorda, " Resolving single cone inputs to visual receptive fields," Nature Neuroscience, 28 June 2009

2008

Delphine D'ebarre, Edward J. Botcherby, Martin J. Booth, and Tony Wilson, "Adaptive optics for structured illumination microscopy," University of Oxford, (2008)

O. Keskin, R. Conan, P. Hampton, C. Bradley, "Derivation and experimental evaluation of a point-spread-function reconstruction from a dual-deformable-mirror adaptive optics system," Optical Engineering, 2008

Robert J. Zawadzki, Barry Cense, Yan Zhang, Stacey S. Choi, Donald T. Miller, and John S. Werner, "Ultrahigh-resolution optical coherence tomography with monochromatic and chromatic aberration correction," Optics Express, Vol. 16, Issue 11, pp. 8126-8143

Daniel X. Hammer, Nicusor V. Iftimia, R. Daniel Ferguson, Chad E. Bigelow, Teoman E. Ustun, Amber M. Barnaby, and Anne B. Fulton, "Foveal Fine Structure in Retinopathy of Prematurity: An Adaptive Optics Fourier Domain Optical Coherence Tomography Study," The Association for Research in Vision and Ophthalmology, Inc., (2008)

Keyvan Sayyah, David M. Pepper, "Dynamic optical tag communicator and system using corner cube modulating retroreflector," 2008

A. Leray, K. Lillis and J. Mertz, "Enhanced Background Rejection in Thick Tissue with Differential-Aberration Two-Photon Microscopy," The Biophysical Society, (2008)

Robert D. Peters, Oliver. P. Lay, and Muthu Jeganathan, "Broadband phase and intensity compensation with a deformable mirror for an interferometric nuller," Applied Optics, Vol. 47, Issue 21, pp. 3920-3926

Huanqing Guo, David A. Atchison, Benjamin J. Birt, "Changes in through-focus spatial visual performance with adaptive optics correction of monochromatic aberrations,"Vision Research Volume 48, Issue 17, August 2008, pp. 1804-1811

Zhangyi Zhong, Benno L. Petrig, Xiaofeng Qi, and Stephen A. Burns , "In vivo measurement of erythrocyte velocity and retinal blood flow using adaptive optics scanning laser ophthalmoscopy," Optics Express, Vol. 16, Issue 17, pp. 12746-12756

Toco Yuen Ping Chui, HongXin Song, and Stephen A. Burns, "Individual variations in human cone photoreceptor packing density: variations with refractive error," 2008

Lisa A. Poyneer, Daren Dillon, Sandrine Thomas, and Bruce A. Macintosh, " Laboratory demonstration of accurate and efficient nanometer-level wavefront control for extreme adaptive optics," Applied Optics, Vol. 47, Issue 9, pp. 1317-1326, (2008)

JI Morgan, JJ Hunter, B Masella, R Wolfe, DC Gray, WH Merigan, FC Delori, DR Williams, "Light-induced retinal changes observed with high-resolution autofluorescence imaging of the retinal pigment epithelium," Invest Ophthalmol Vis Sci., (2008)

Nicholas Devaney, Derek Coburn, Chris Coleman, J. Christopher Dainty, Eugenie Dalimier, Thomas Farrell, David Lara, David Mackey, and Ruth Mackey, "Characterisation of MEMs mirrors for use in atmospheric and ocular wavefront correction," Proc. SPIE, Vol. 6888

Julia W. Evans, Robert J. Zawadzki, Steve Jones, Samelia Okpodu, Scot Olivier, John S. Werner, "Performance of a MEMS-based AO-OCT system," Proc. SPIE, Vol. 6888, (2008)

Benjamin Potsaid and John Ting-Yung Wen, "Design of Adaptive Optics Based Systems by Using MEMS Deformable Mirror Models," International Journal of Optomechatronics, Volume 2, Issue 2 April 2008, pages 104 – 125

T.D. Farrel and J.C. Dainty, "Woofer-Tweeter Adaptive Optics" 2008

P. Bierden, " MEMS Deformable Mirrors for High Performance AO Applications," 2008

2007

N. Jeremy Kasdin, Robert J. Vanderbei, and Ruslan Belikov, "Shaped pupil coronagraphy," Comptes Rendus Physique, Volume 8, Issues 3-4, pp. 312-322 (2007)

Pircher, Michael; Zawadzki, Robert J, " Combining adaptive optics with optical coherence tomography: unveiling the cellular structure of the human retina in vivo," Expert Review of Ophthalmology, Volume 2, Number 6, pp. 1019-1035 (2007)

Delphine Debarre, Martin J. Booth, and Tony Wilson, "Image based adaptive optics through optimisation of low spatial frequencies," Optics Express, Vol. 15, Issue 13, pp. 8176-8190

J.K. Wallace, B. Macintosh, M. Shao, R. Bartos, P. Dumont, B.M. Levine, S. Rao, R. Samuele, C. Shelton, "An Interferometric Wave Front Sensor for Measuring Post-Coronagraph Errors on Large Optical Telescopes," Aerospace Conference, pp. 1-7, (2007)

Amir Give'on, Ruslan Belikov, Stuart Shaklan, and Jeremy Kasdin , "Closed loop, DM diversity-based, wavefront correction algorithm for high contrast imaging systems," Optics Express, Vol. 15, Issue 19, pp. 12338-12343

Daniel X. Hammer, Nicusor V. Iftimia, Chad E. Bigelow, Teoman E. Ustun, Benjamin Bloom, R. Daniel Ferguson, Stephen A. Burns, "High resolution retinal imaging with a compact adaptive optics spectral domain optical coherence tomography system," Vol. **6426, (2007)**

David A. Horsley , Hyunkyu Park, Sophie P. Laut and John S. Werner , "Characterization of a bimorph deformable mirror using stroboscopic phase-shifting interferometry," Sensors and Actuators A: Physical, Volume 134, (2007), Pages 221-230

Alfredo Dubra , "Wavefront sensor and wavefront corrector matching in adaptive optics," Optics Express, Vol. 15, Issue 6, pp. 2762-2769

Jacque L. Duncan, Yuhua Zhang, Jarel Gandhi, Chiaki Nakanishi, Mohammad Othman, Kari E. H. Branham, Anand Swaroop, and Austin Roorda, "High-Resolution Imaging with Adaptive Optics in Patients with Inherited Retinal Degeneration," Invest Ophthalmol Vis Sci. 2007

Diana C. Chen, Steven M. Jones, Dennis A. Silva, and Scot S. Olivier , "High-resolution adaptive optics scanning laser ophthalmoscope with dual deformable mirrors," JOSA A, Vol. 24, Issue 5, pp. 1305-1312

Gordon T. Kennedy, Carl Paterson, "Correcting the ocular aberrations of a healthy adult population using microelectromechanical (MEMS) deformable mirrors," Optics Communications, Volume 271, Pages 278-284, (2007)

Bruce Macintosha, James Grahama, David Palmera, Rene Doyond, Don Gavela, James Larkina, Ben Oppenheimera, Leslie Saddlemyerh, J. Kent Wallacea, Brian Baumana, Darren Eriksonh, Lisa Poyneera, Anand Sivaramakrishnana, Rémi Soummera, and Jean-Pierre Veranh, "Adaptive optics for direct detection of extrasolar planets: the Gemini Planet Imager," Comptes Rendus Physique, Volume 8, pp. 365-373, (2007)

2006

Michael Shao, Bruce M. Levine, James K. Wallace, Glenn S. Orton, Edouard Schmidtlin, Benjamin F. Lane, Sara Seager, Volker Tolls, Richard G. Lyon, Rocco Samuele, Domenick J. Tenerelli, Robert Woodruff, Jian Ge, "A nulling coronagraph for TPF-C," Proc. SPIE, Vol. 6265, (2006)

Robert D. Peters, Oliver P. Lay, Akiko Hirai, and Muthu Jeganathan, "Adaptive nulling for the Terrestrial Planet Finder Interferometer," Proc. SPIE, Vol. 6268, (2006)

Volker Tolls, Michael Aziz, Robert A. Gonsalves, Sylvain Korzennik, Antoine Labeyrie, Richard Lyon, Gary Melnick, Ruth Schlitz, Steve Somerstein, Gopal Vasudevan, and Robert Woodruff, "Study of coronagraphic techniques," Proc. SPIE, Vol. 6265, (2006)

Elizabeth Daly, Eugenie Dalimier, and Chris Dainty, "Requirements for MEMS mirrors for adaptive optics in the eye," 2006

Bruce Macintosh, Katie Morzinski, Dave Palmer and Lisa Poyneer, "The extreme adaptive optics testbed at UCSC: current results and coronagraphic upgrade," Proc. SPIE, Vol. **6272**, (2006)

Aymeric Leray and Jerome Mertz, "Rejection of two-photon fluorescence background in thick tissue by differential aberration imaging," Optics Express, Vol. 14, Issue 22, pp. 10565-10573

Yuhua Zhang, Siddharth Poonja, and Austin Roorda, "AOSLO: from benchtop to clinic," Proc. SPIE, Vol. 6306, (2006)

Steven A. Cornelissen, Paul A. Bierden, Steven Menn and Thomas G. Bifano, "A 4096-element micromirror for high-contrast astronomical imaging," Proc. SPIE, 2006

Katie M. Morzinski, Julia W. Evans, Scott Severson, Bruce Macintosh, Daren Dillon, Don Gavel, Claire Max, and Dave Palmer, "Characterizing the potential of MEMS deformable mirrors for astronomical adaptive optics," Proc. SPIE, Vol. 6272, (2006)

Brian P. Wallace, Peter J. Hampton, Colin H. Bradley and Rodolphe Conan, "Evaluation of a MEMS deformable mirror for an adaptive optics test bench," Optics Express, Vol. 14, Issue 22, pp. 10132-10138

B. Potsaid, J.T. Wen, Automation of Challenging Spatial-Temporal Biomedical Observations with the Adaptive Scanning Optical Microscope (ASOM), pp. 8-10 Oct. 2006.

Julia W. Evans, Bruce Macintosh, Lisa Poyneer, Katie Morzinski, Scott Severson, Daren Dillon, Donald Gavel, and Layra Reza, " Demonstrating sub-nm closed loop MEMS flattening," Optics Express, Vol. 14, Issue 12, pp. 5558-5570, 2006.

Daniel X. Hammer, R. Daniel Ferguson, Chad E. Bigelow, Nicusor V. Iftimia, Teoman E. Ustun, and Stephen A. Burns, Adaptive optics scanning laser ophthalmoscope for stabilized retinal imaging, Optics Express, Vol. 14, Issue 8, pp. 3354-3367, 2006.

L Abe, M. Tamura, T. Nakagawa, K. Enya, S. Tanaka, K. Fujita, J. Nishikawa, N. Murakami, and H. Kataza, "Current status of the coronagraphic mode for the 3.5m SPICA space telescope," Proceedings of the IAU Colloquium #200, pp. 329-334, 2006.

Onur Keskin, Peter Hampton, Rodolphe Conan, Colin Bradleyk, Aaron Hilton, and Celia Blain, " Woofer-Tweeter Adaptive Optics Test Bench," First NASA/ESA Conference on Adaptive Hardware and Systems, pp. 74-80, 2006.

Curtis R. Vogel and Qiang Yang, Modeling, simulation, and open-loop control of a continuous facesheet MEMS deformable mirror," Journal of the Optical Society of America A, Vol. 23, Issue 5, pp. 1074-1081, 2006.

Jason B. Stewart, Thomas G. Bifano, Paul Bierden, Steven Cornelissen, Timothy Cook, and B. Martin Levine, Design and development of a 329-segment tip-tilt piston mirrorarray for space-based adaptive optics," Proceedings of SPIE, Vol. 6113, pp. 181-189, 2006.

Keigo Enya, Takao Nakagawa, Hirokazu Kataza, Hidehiro Kaneda, Yukari Yamashita Yui, Motohide Tamura, Lyu Abe, Yoshiyuki Obuchi, Takashi Miyata, Shigeyuki Sako, Takashi Onaka, and Hidenori Takahashi, Cryogenic infrared optics for SPICA coronagraph," Proceedings of the IAU Colloquium #200, pp. 467-472, 2006.

Alexandros Papavasiliou and Scot Olivier, Nanolaminate foils used to make deformable mirrors," SPIE Newsroom, 2006.

R. Daniel Ferguson, Daniel X. Hammer, Chad E. Bigelow, Nicusor V. Iftimia, Teoman E. Ustun, Stephen A. Burns, Ann E. Elsner, and David R. Williams, Tracking adaptive optics scanning laser ophthalmoscope," Proceedings of SPIE, Vol. 6138, pp. 232-240, 2006.

Daniel X. Hammer, R. Daniel Ferguson, Chad E. Bigelow, Nicusor V. Iftimia, Teoman E. Ustun, Gary D. Noojin, David J. Stolarski, Harvey M. Hodnett, Michelle L. Imholte, Semih S. Kumru, Michelle N. McCall, Cynthia A. Toth, and Benjamin A. Rockwell, Precision targeting with a tracking adaptive optics scanning laser ophthalmoscope," Proceedings of SPIE, Vol. 6138, pp. 241-250, 2006.

Yuhua Zhang, Siddharth Poonja, and Austin Roorda, "Adaptive optics scanning laser ophthalmoscope using a micro-electro-mechanical (MEMS) deformable mirror," Proceedings of SPIE, Vol. 6138, pp. 221-231, 2006.

J. W. Evans, K. Morzinski, S. Severson, L. Poyneer, B. Macintosh, D. Dillon, L. Reza, D. Gavel, D. Palmer, S. Olivier, and P. Bierden, Extreme Adaptive Optics Testbed: Performance and Characterization of a 1024 Deformable Mirror," Proceedings of SPIE, Vol. 6113, pp. 131-136, 2006.

Yaopeng Zhou and Thomas Bifano, Characterization of contour shapes achievable with a MEMS deformable mirror," Proceedings of SPIE, Vol. 6113, pp. 123-130, 2006.

Robert J. Zawadzki, Steven M. Jones, Mingtao Zhao, Stacey S. Choi, Sophie S. Laut, Scot S. Olivier, Joseph A. Izatt, and John S. Werner, Adaptive optics-optical coherence tomography for in vivo retinal imaging: comparative analysis of two wavefront correctors," Proceedings of SPIE, Vol. 6079, pp. 38-46, 2006.

Hide 12 x 12 Array Deformable Mirror, 15 Hz CCD Wavefront Sensor

12 x 12 Array Deformable Mirror, 15 Hz CCD Wavefront Sensor

Part Number	Description	Price	Availability
AOK1-UM01	Adaptive Optics Kit with Gold-Coated Multi-DM (140 Actuators)	$23,000.00	Today
AOK1-UP01	Adaptive Optics Kit with Aluminum-Coated Multi-DM (140 Actuators)	$23,000.00	Lead Time

Hide 6 x 6 Array Deformable Mirror, 15 Hz CCD Wavefront Sensor

6 x 6 Array Deformable Mirror, 15 Hz CCD Wavefront Sensor

Part Number	Description	Price	Availability
AOK2-UM01	Adaptive Optics Kit with Gold-Coated Mini-DM (32 Actuators)	$12,000.00	Lead Time

Hide 12 x 12 Array Deformable Mirror, 880 Hz CMOS Wavefront Sensor

12 x 12 Array Deformable Mirror, 880 Hz CMOS Wavefront Sensor

Part Number	Description	Price	Availability
AOK5-UM01	NEW! Adaptive Optics Kit with Gold-Coated Multi-DM (140 Actuators) and Fast Shack-Hartmann WFS	$25,950.00	Lead Time
AOK5-UP01	NEW! Adaptive Optics Kit with Aluminum-Coated Multi-DM (140 Actuators) and Fast Shack-Hartmann WFS	$25,950.00	Lead Time

Visit the *Adaptive Optics Kits* page for pricing and availability information:
http://www.thorlabs.com/newgrouppage9.cfm?objectgroup_id=3208